The Development of a Partially Averaged Navier-Stokes KSKL Model

Klapwijk, Maarten; Lloyd, Thomas; Vaz, Guilherme

DOI
10.1115/1.4052484

Publication date
2022

Document Version
Final published version

Published in
Journal of Fluids Engineering, Transactions of the ASME

Maarten Klapwijk
Maritime and Transport Technology,
Faculty of Mechanical, Maritime and
Material Engineering (3mE),
Delft University of Technology,
Mekelweg 2,
Delft 2628 CN, The Netherlands;
Maritime Research Institute Netherlands
(MARIN),
Haagsteeg 2,
Wageningen 6708 PM, The Netherlands
e-mail: M.D.Klapwijk@tudelft.nl

Thomas Lloyd
Ships Department,
Maritime Research Institute Netherlands
(MARIN),
Haagsteeg 2,
Wageningen 6708 PM, The Netherlands
e-mail: T.Lloyd@marin.nl

Guilherme Vaz
BlueOasis,
Quinta da Fonte—Rua dos Malhões,
Edifício D. Pedro I,
Lisbon 2770-071, Portugal
e-mail: gvaz@blueoasis.pt

The Development of a Partially Averaged Navier–Stokes KSKL Model

A new partially averaged Navier–Stokes (PANS) closure is derived based on the $k-\sqrt{k}L$ (KSKL) model. The aim of this new model is to incorporate the desirable features of the KSKL model, compared to the $k-\omega$ shear stress transport model, into the PANS framework. These features include reduced eddy-viscosity levels, a lower dependency on the cell height at the wall, well-defined boundary conditions, and improved iterative convergence. As well as the new model derivation, the paper demonstrates that these desirable features are indeed maintained, for a range of modeled-to-total turbulence kinetic energy ratios (f_k), and even for multiphase flow.
[DOI: 10.1115/1.4052484]

1 Introduction

The prediction of turbulent flows has been under investigation for decades (see Refs. [1–4] for an overview). Increasing available computational power has shifted the focus in research for engineering (high Reynolds) flows toward scale resolving simulations (SRS). In SRS, the larger scales of turbulence are resolved, with the smaller scales modeled. This is in contrast to the current workhorse of industry, Reynolds-averaged Navier–Stokes (RANS), where the full turbulence spectrum is modeled. The increase in available computational power during the last decades makes the use of SRS possible for high Reynolds number flows. The added physical resolution should lead to a more accurate description of the flow and a reduction of the modeling error at a reasonable cost. For SRS, several methods exist, such as large eddy simulation (LES) [5], "hybrid" methods, such as detached eddy simulation [6], and "bridging" methods, such as partially averaged Navier–Stokes (PANS) [7,8]. Bridging methods consist of a blending of RANS and direct numerical simulation (DNS), but, in contrast to hybrid methods, the blending is not location dependent. Instead, it depends on user-defined settings, such as the ratio of modeled-to-total turbulence kinetic energy f_k.

In PANS, the filter between RANS and DNS is set a priori, leading to the theoretical advantage that the numerical and modeling errors are decoupled, as long as f_k is kept constant in time and space [9–11]. The use of a single formulation ranging from RANS to DNS prevents ad hoc behavior when switching between resolving and modeling turbulence, as can occur for hybrid methods [11]. The closure of the equations relies on a RANS parent model. In the literature, several different closure methods can be found. Similar to RANS modeling, common two-equation PANS closures are based on either $k-\varepsilon$ models (e.g., Refs. [12–17]) or the closely related $k-\omega$ models (e.g., Refs. [9,18–20]). Interesting recent developments are the use of a nonlinear closure as PANS model (e.g., Refs. [21] and [22]). Alternative methods are based on more equation RANS models such as Refs. [23–25]. The latter methods are promising, but from a literature survey, there appears to be a preference for the use of two-equation methods from an engineering perspective. While decent results have been obtained using $k-\varepsilon$ and $k-\omega$ models, these do have several issues which we will comment upon later. In this study, we derive a new PANS model based on the $k-\sqrt{k}L$ (KSKL) model [26].

Why do we need another PANS closure model? For RANS modeling, in the maritime field, there is a preference for $k-\omega$ models [27]. Yet we know that there are several theoretical and practical advantages to prefer the KSKL model over $k-\omega$-based models. First, the KSKL model commonly predicts lower eddy viscosities compared to $k-\omega$ models (see, e.g., Refs. [26,28,29]). This has favorable consequences for multiphase and cavitating flow predictions. In such cases, often dynamics are suppressed by excessive eddy-viscosity levels. In the context of PANS, this property is expected to be maintained for varying f_k values. Second, the RANS KSKL model exhibits a lower dependency on the height of the first near-wall cell ($y^+ = u_\tau y/\nu$, with u_τ the wall friction velocity, y the cell height, and ν the kinematic viscosity), thereby resulting in decreased numerical errors on the same grid [30]. Thirdly, $k-\omega$ models suffer from difficult to define boundary conditions at the outer boundary, and at the wall, where ω goes to infinity [31]. In contrast, $\sqrt{k}L$ is zero by definition at the wall, making it easier to implement in CFD codes and also improving iterative convergence. Finally, one of the shortcomings of $k-\omega$-based models is the generally poor iterative convergence of the second transport equation for the dissipation rate ω, especially in connection with multiphase problems, such as cavitation and free-surface flows (see, e.g., Refs. [29,32–36]. When combining a $k-\omega$ with the PANS framework, this feature is incorporated. This leads to non-negligible iterative errors even for simulations with a high physical resolution (i.e., close to DNS), while in this case it would be reasonable to expect the Discretization error to be the dominating error source in the total numerical error. In such cases, the RANS parent model only works as a subfilter model, of which it would be desirable to be accompanied by a

Contributed by the Fluids Engineering Division of ASME for publication in the Journal of Fluids Engineering. Manuscript received May 28, 2021; final manuscript received September 15, 2021; published online January 12, 2022. Assoc. Editor: Qianhong Wu.

small iterative error. Large iterative errors also make the estimation of Discretization errors difficult—which is one of the main attractions of PANS [9,11]—since for such methods the iterative error should be at least two orders of magnitude lower than the Discretization error [37]. The PANS-KSKL model is expected to exhibit, like its RANS counterpart, improved iterative convergence behavior due to the substitution of the ω equation by the $\sqrt{k}L$ equation. These properties have motivated other researchers to also favor the KSKL model, for example, in the context of transition modeling [38] and the prediction of drag forces [39].

In this paper, first the PANS-KSKL model derivation is presented, followed by an investigation into the model behavior based on two example flows: a turbulent channel flow and an elliptical wing exhibiting a cavitating tip vortex. In this work, the focus is on simulating both cases with low f_k values, to investigate the behavior of the KSKL model, working as a subfilter model in PANS. The flows are simulated using the open-usage finite volume, face-based, CFD code, REFRESCO [40]. It predicts multiphase, unsteady, incompressible viscous flows using the Navier–Stokes equations, complemented with a range of turbulence and cavitation models.

2 Partially Averaged Navier–Stokes k–$\sqrt{k}L$ Model Derivation

In SRS, the instantaneous quantities, Φ, are decomposed into a resolved, $\langle\Phi\rangle$, and a modeled (unresolved) component, ϕ, according to $\Phi = \langle\Phi\rangle + \phi$ [41]. Applying this decomposition to the equations of mass and momentum conservation for an incompressible Newtonian fluid, written in tensor form, including phase change, yields

$$\frac{\partial\langle U_i\rangle}{\partial x_i} = \frac{\dot{m}}{\rho_v} \quad (1)$$

and

$$\frac{\partial(\rho\langle U_i\rangle)}{\partial t} + \frac{\partial}{\partial x_j}\cdot(\rho\langle U_i\rangle\langle U_j\rangle) = -\frac{\partial P}{\partial x_i} + \frac{\partial}{\partial x_j}\left[\mu\left(\frac{\partial\langle U_i\rangle}{\partial x_j} + \frac{\partial\langle U_j\rangle}{\partial x_i} - \frac{2}{3}\frac{\partial\langle U_m\rangle}{\partial x_m}\delta_{ij}\right)\right] + \frac{\partial\tau_{ij}}{\partial x_j} \quad (2)$$

In these equations, U_i denotes the velocity components, P is the static pressure, μ is the dynamic viscosity (with $\mu = \rho\nu$, where ν is the kinematic viscosity), and ρ is the density. In the context of cavitation modeling, we employ the volume of fluid [42] approach, where a single set of mass and momentum equations is solved for the homogeneous mixture. The source term $\dot{m}$, describing phase change, is computed using a mass transfer model [32], based on the Schnerr–Sauer cavitation model [43]. Symbols without subscript refer to the mixture quantities, defined according to

$$\rho = \alpha_v\rho_v + (1-\alpha_v)\rho_l \quad \text{and} \quad \nu = \alpha_v\nu_v + (1-\alpha_v)\nu_l \quad (3)$$

where $\alpha_v = V_v/(V_v + V_l)$ denotes the vapor volume fraction, with V indicating the phase volume. Subscripts l and v refer to the liquid and vapor phase, respectively. τ_{ij} denotes the modeled Reynolds stress tensor, which is computed using Boussinesq's hypothesis

$$\frac{\tau_{ij}}{\rho} = \langle U_iU_j\rangle - \langle U_i\rangle\langle U_j\rangle = 2\nu_t\langle S_{ij}\rangle - \frac{2}{3}k\delta_{ij} \quad (4)$$

with ν_t is the eddy viscosity, k is the modeled turbulence kinetic energy, δ_{ij} is the Kronecker delta, and $\langle S_{ij}\rangle$ is the resolved strain rate tensor, defined as

$$\langle S_{ij}\rangle = \frac{1}{2}\left(\frac{\partial\langle U_i\rangle}{\partial x_j} + \frac{\partial\langle U_j\rangle}{\partial x_i}\right) \quad (5)$$

In the derivation of the PANS model, following literature, we employ the ratio of modeled-to-total turbulence kinetic energy, $f_k = k/K$, for the first equation. Throughout this derivation, uppercase letters indicate the total, i.e., RANS quantity, while lowercase letters indicate the modeled, i.e., PANS quantity. So K is the RANS turbulence kinetic energy, while k is the modeled turbulence kinetic energy in PANS. For the second equation, which solves for $\sqrt{k}L$, we define the secondary ratio based on the modeled turbulent integral length scale L, as

$$f_l = \frac{l}{L} \quad (6)$$

In Sec. 3.1, we will elaborate on this choice.

2.1 k Equation

The k equation is given by

$$\frac{\partial(K)}{\partial t} + \frac{\partial}{\partial x_j}\cdot(K\langle U_j\rangle) = P_K - D_K + \frac{\partial}{\partial x_j}\left[(\nu + \nu_{tT}c_{\sigma_k})\frac{\partial k}{\partial x_j}\right] \quad (7)$$

with the production and destruction terms for the KSKL model defined as

$$P_K = \nu_{tT}\langle S\rangle^2 \quad \text{and} \quad D_K = C_\mu^{3/4}\frac{K^{3/2}}{L} \quad (8)$$

Here, $c_{\sigma_k} = 1/\sigma_k$ and $\langle S\rangle$ is the magnitude of the strain rate tensor $\langle S\rangle = 2\langle S_{ij}\rangle\langle S_{ij}\rangle$. All constants, such as σ_k and C_μ, are given in Table 1. ν_t indicates the eddy viscosity in PANS, while ν_{tT} denotes the RANS eddy viscosity.

The derivation is based on the relation between RANS and PANS turbulence kinetic energy, which is given by

$$\frac{\partial(k)}{\partial t} + \frac{\partial}{\partial x_j}\cdot(k\langle\overline{U_j}\rangle) = f_k\left[\frac{\partial(K)}{\partial t} + \frac{\partial}{\partial x_j}\cdot(K\langle\overline{U_j}\rangle)\right] \quad (9)$$

and can be rewritten as

$$\frac{\partial(k)}{\partial t} + \frac{\partial}{\partial x_j}\cdot(k\langle U_j\rangle) = f_k\left[\frac{\partial(K)}{\partial t} + \frac{\partial}{\partial x_j}\cdot(K\langle\overline{U_j}\rangle)\right] + \frac{\partial(k)}{\partial t} + \frac{\partial}{\partial x_j}\cdot\left[\left(k\left(\langle U_j\rangle - \langle\overline{U_j}\rangle\right)\right]\right. \quad (10)$$

When we replace conservation expressions on the left and right by the closure equation, we obtain

$$P_k - D_k + \frac{\partial}{\partial x_j}\left[(\nu + \nu_t c_{\sigma_k})\frac{\partial k}{\partial x_j}\right] = f_k\left[P_K - D_K + \frac{\partial}{\partial x_j}\left[(\nu + \nu_{tT}c_{\sigma_k})\frac{\partial K}{\partial x_j}\right]\right] + \frac{\partial}{\partial x_j}\cdot\left[\left(k\left(\langle U_j\rangle - \langle\overline{U_j}\rangle\right)\right]\right. \quad (11)$$

Table 1 Coefficients of the KSKL turbulence model

a_1^R	a_1^S	c_{d_1}	c_{l_1}	c_{l_2}	C_μ	κ	σ_k	$\sigma_{\sqrt{k}l}$	ζ_1	ζ_2	ζ_3
0.577	0.320	4.700	10.000	1.300	0.090	0.410	2/3	2/3	0.800	1.470	0.0288

For the local terms, the following relationship holds

$$P_k - D_k = f_k[P_K - D_K] \tag{12}$$

implying that

$$P_K = \frac{1}{f_k}(P_k - D_k) + D_K \tag{13}$$

Following the zero transport model approach, where it is assumed that the resolved fluctuating velocity field does not contribute to the turbulent transport of the modeled field, the last term $(\frac{\partial}{\partial x_j} \cdot [k(\langle U_j \rangle - \langle \overline{U_j} \rangle)])$ is assumed to be zero. When Eq. (13) is inserted in Eq. (11), after moving f_k to the left-hand side, we obtain

$$\frac{\partial(k)}{\partial t} + \frac{\partial}{\partial x_j} \cdot \left(k\langle U_j \rangle\right) = P_k - D_k + \frac{\partial}{\partial x_j}\left[\left(\nu + \nu_{tT} c_{\sigma_k}\right)\frac{\partial k}{\partial x_j}\right] \tag{14}$$

Based on the definition of the eddy viscosity

$$\nu_t = \min\left(C_\mu^{1/4}\sqrt{kl}; \frac{a_1 k}{\langle S \rangle}\right) \tag{15}$$

the ratios of the RANS and PANS eddy viscosities can be expressed in terms of f_k and f_l:

$$\nu_{tT} = \frac{1}{\sqrt{f_k f_l}}\nu_t \tag{16}$$

Combining Eq. (15) with Eq. (14) leads to the PANS k equation

$$\frac{\partial(k)}{\partial t} + \frac{\partial}{\partial x_j} \cdot \left(k\langle U_j \rangle\right) = P_k - D_k + \frac{\partial}{\partial x_j}\left[\left(\nu + \frac{\nu_t}{\sigma_k \sqrt{f_k f_l}}\right)\frac{\partial k}{\partial x_j}\right] \tag{17}$$

2.2 $\sqrt{kl}$ Equation

The KSKL $\sqrt{kl}$ equation is given by

$$\begin{aligned}\frac{\partial(\sqrt{\mathrm{KL}})}{\partial t} + \frac{\partial}{\partial x_j} \cdot \left(\sqrt{\mathrm{KL}}\langle U_j \rangle\right) &= \frac{\sqrt{\mathrm{KL}}}{K}\nu_{tT}\langle S \rangle^2\left(\zeta_1 - \zeta_2\left(\frac{L}{L_{vk}}\right)^2\right) \\ &\quad - \zeta_3 K + \frac{\partial}{\partial x_j}\left[\left(\nu + \frac{\nu_{tT}}{\sigma_{\sqrt{\mathrm{KL}}}}\right)\frac{\partial(\sqrt{\mathrm{KL}})}{\partial x_j}\right] \\ &\quad - 6\nu\frac{\sqrt{\mathrm{KL}}}{d^2}F_{\sqrt{kl}}\end{aligned} \tag{18}$$

with the von Kármán length scale defined as

$$L_{vk} = \max\left(\min\left(\frac{\kappa\langle S \rangle}{\sqrt{\frac{\partial^2\langle U_i \rangle}{\partial x_k^2}\frac{\partial^2\langle U_i \rangle}{\partial x_j^2}}}; c_{l_2}\kappa d\right); \frac{L}{c_{l_1}}\right) \tag{19}$$

where d indicates the near wall distance. We again relate RANS to PANS

$$\frac{\partial(\sqrt{kl})}{\partial t} + \frac{\partial}{\partial x_j} \cdot \left(\sqrt{kl}\langle \overline{U_j} \rangle\right) = \sqrt{f_k f_l}\left[\frac{\partial(\sqrt{\mathrm{KL}})}{\partial t} + \frac{\partial}{\partial x_j} \cdot \left(\sqrt{\mathrm{KL}}\langle \overline{U_j} \rangle\right)\right] \tag{20}$$

which can be rewritten as

$$\begin{aligned}\frac{\partial(\sqrt{kl})}{\partial t} + \frac{\partial}{\partial x_j} \cdot \left(\sqrt{kl}\langle U_j \rangle\right) &= \sqrt{f_k f_l}\left[\frac{\partial(\sqrt{\mathrm{KL}})}{\partial t} + \frac{\partial}{\partial x_j} \cdot \left(\sqrt{\mathrm{KL}}\langle \overline{U_j} \rangle\right)\right] \\ &\quad + \frac{\partial}{\partial x_j} \cdot \left[\sqrt{kl}\left(\langle U_j \rangle - \langle \overline{U_j} \rangle\right)\right]\end{aligned} \tag{21}$$

Next, we replace the conservation expression on the right-hand side by the KSKL closure, and again apply the zero transport assumption. To relate all quantities to known, subfilter, quantities, L is replaced by l/f_l. After simplification, the PANS $\sqrt{kl}$ equation is obtained

$$\begin{aligned}\frac{\partial(\sqrt{kl})}{\partial t} + \frac{\partial}{\partial x_j} \cdot \left(\sqrt{kl}\langle U_j \rangle\right) &= \frac{\sqrt{f_k}\sqrt{kl}}{f_l k}\nu_t\langle S \rangle^2\left(\zeta_1 - \zeta_2\left(\frac{l}{f_l L_{vk}}\right)^2\right) \\ &\quad - \zeta_3 k\frac{f_l}{\sqrt{f_k}} + \frac{\partial}{\partial x_j}\left[\left(\nu + \frac{\nu_t}{\sigma_{\sqrt{kl}}\sqrt{f_k f_l}}\right)\right. \\ &\quad \left. \times \frac{\partial(\sqrt{kl})}{\partial x_j}\right] - 6\nu\frac{\sqrt{kl}}{d^2}F_{\sqrt{kl}}\end{aligned} \tag{22}$$

In line with the approach by Ref. [9], the auxiliary functions are kept equal to the formulations from the RANS model for several reasons. Firstly, this ensures that the model performs as the RANS parent model for $f_k = 1.0$. These auxiliary functions relate to the subfilter quantities, which implies that they should be independent on f_k and f_l. Also, these relations are tuned for a RANS models. When introducing f_k and f_l, these relations should ideally be retuned, for varying f_k values, which currently is considered out of the scope of this work. Also note that the effect of these relations will decrease with lowering f_k. The functions are

$$a_1 = a_1^S f_b + (1 - f_b)a_1^R \tag{23}$$

$$f_b = \tanh\left[\left(\frac{20\left(C_\mu^{1/4}\sqrt{kl} + \nu\right)}{\kappa^2\langle S \rangle^2 d^2 + 0.01\nu}\right)^2\right] \tag{24}$$

$$F_{\sqrt{kl}} = \frac{1 + c_{d_1}\xi}{1 + \xi^4} \tag{25}$$

and

$$\xi = \frac{\sqrt{0.3k}d}{20\nu} \tag{26}$$

3 Partially Averaged Navier–Stokes k–$\sqrt{kL}$ Model Properties

3.1 Specifying f_l. The filtering of the Navier–Stokes equations depends on the values chosen for the ratios of modeled-to-total quantities. In the context of two-equation models, two parameters are needed. While the choice for the k equation is trivial (namely, f_k), for the secondary equation an obvious choice would have been $f_{\sqrt{kl}} = \sqrt{kl}/(\sqrt{\mathrm{KL}})$. However, this presents two problems. Firstly, there is the interpretation: in the original version of PANS, f_k determines the physical resolution of the flow, i.e., to what extent the turbulence spectrum is resolved; while the second setting $f_\varepsilon = \varepsilon/E$ determines the overlap between the energy-containing and the dissipation ranges. In contrast, it is not immediately clear what the quantity $\sqrt{kl}$ represents—even in the RANS parent model—and consequently the interpretation of $f_{\sqrt{kl}}$. Secondly, there is the problematic feature that $f_{\sqrt{kl}}$ directly couples the first and secondary setting of the PANS model, since the

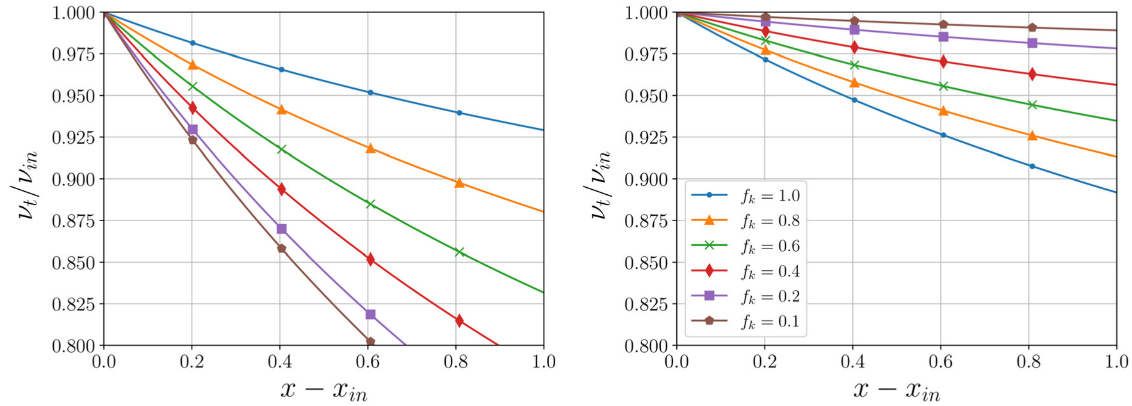

Fig. 1 Decay of ν_t versus downstream location x as function of f_k for PANS-SST (left) and PANS-KSKL (right) according to Eqs. (30) and (31), respectively. Values used for this example are $C_\mu = 0.09$, $\beta^* = 0.09$, $\alpha = 0.5$, $\zeta_3 = 0.028$, $\beta = 0.08$, $\langle U\rangle = 1.0$, $k_{\text{in}}/\nu_{t,\text{in}} = 10$.

secondary equation also solves for a term depending on k. In the RANS formulation (see Ref. [26]), this property is obscured by the fact that $\sqrt{\text{KL}}$ is commonly designated Φ. In the context of PANS, a consequence of this choice would be that varying f_k will directly affect $f_{\sqrt{kl}}$. For these reasons, employing f_l is preferred.

As mentioned before, the original version of PANS is based on f_k and f_ε. For ease of use it is preferable to have the same two settings for different types of PANS closures. Consequently, for $k-\omega$ based PANS models, the second parameter f_ω is related to f_ε (see, e.g., Ref. [9]), using

$$f_\omega = \frac{f_\varepsilon}{f_k} \tag{27}$$

Thereby the user needs to set f_k and f_ε, and the appropriate f_ω is selected in the code.

In the case of PANS-KSKL, following the relationship derived by Ref. [44], the PANS length scales can be related to the RANS length scales using

$$\frac{l}{L}(=f_l) \sim \frac{f_k^{3/2}}{f_\varepsilon} \tag{28}$$

This can also be derived when combining Eq. (16) with the ratio of eddy viscosities [44]

$$\frac{\nu_t}{\nu_{tT}} = \frac{f_k^2}{f_\varepsilon} \tag{29}$$

3.2 Implications for Subfilter Quantities. The sole effect of the subfilter model on the filtered Navier–Stokes equations is on the eddy viscosity, the formulation of which varies between the $k-\omega$ and KSKL closures. As mentioned in the introduction, for RANS, it is commonly observed that the eddy viscosities predicted by the KSKL model are lower than those of $k-\omega$ models. This should hold when using PANS-KSKL with $f_k < 1.0$.

A related property is that the decay in ν_t, downstream of the inlet, is affected by the closure formulation. We know from RANS modeling that the location of transition strongly depends on the turbulence quantities, and therefore on the decay of ν_t from the inlet (see, e.g., Refs. [45] and [46]). This effect is limited for RANS simulations of high Reynolds number flows, where a "fully turbulent" solution is assumed, but its relative importance increases with decreasing Reynolds number. In the context of SRS, the effect of $\nu_{t,\text{in}}$ is often overlooked, since with decreasing f_k, the ν_t decreases until 0 in the limit of $f_k = 0.0$ [47]. However, for intermediate values f_k values, $\nu_{t,\text{in}}$ still has an effect on the equations being solved (i.e., Eq. (2)), making the decay a relevant parameter. Following the derivations by Ref. [48] for the RANS shear stress transport (SST) and KSKL model, we can derive the decay of PANS-SST and PANS-KSKL. Under the assumptions of a steady, uniform flow, aligned with the x axis, sufficiently far away from walls, constant f_k in the domain, and by neglecting the diffusion terms, the decay of PANS-SST can be formulated as

$$\nu_t = \frac{\nu_{t,\text{in}}}{\left[\frac{1}{\langle U\rangle}\left(\langle U\rangle + (\alpha\beta^* - \alpha\beta^* f_k + \beta f_k)(x - x_{\text{in}})\frac{k_{\text{in}}}{\nu_{t,\text{in}}}\right)\right]^{\frac{\beta^*}{\alpha\beta^* - \alpha\beta^* f_k + \beta f_k} - 1}} \tag{30}$$

while the decay for PANS-KSKL is

$$\nu_t = \frac{\nu_{t,\text{in}}}{\left[\frac{1}{\langle U\rangle}\left(\langle U\rangle + \beta_{\text{KSKL}}(x - x_{\text{in}})\frac{k_{\text{in}}}{\nu_{t,\text{in}}}\right)\right]^{\frac{\beta^*}{\beta_{\text{KSKL}}} - 1}} \tag{31}$$

with the subscript in indicating values at the inlet of the domain, and

$$\beta_{\text{KSKL}} = \beta^* - \zeta_3 C_\mu^{1/4} f_k \tag{32}$$

Equations (30) and (31) are derived in Appendix A. The solution for the decay of ν_t for PANS-SST and PANS-KSKL model is of a similar form as the solutions for the RANS parent models, but with different constants. These constants do not only depend on the constants of the model but are also a function of f_k. The functions are shown graphically in Fig. 1. Interestingly, the two closures show a different trend. For $f_k = 1.0$ (the RANS models), the KSKL model shows a larger ν_t decay, compared to the SST model. With decreasing f_k, for PANS-SST the decay increases, leading to a large decrease in ν_t downstream of the inlet. For PANS-KSKL, the decay decreases with decreasing f_k, leading to a reduced decay compared to PANS-SST. The f_k for which the decays are equal depends on the values $k_{\text{in}}/\nu_{t,\text{in}}$ and the downstream distance $x - x_{\text{in}}$. In the limit of $f_k = 0.0$, the PANS-KSKL model, theoretically, shows no decay of ν_t. This implies that with decreasing f_k, the PANS-SST model becomes less sensitive to the inlet boundary conditions, while the PANS-KSKL model becomes more sensitive to this, leading to the need to vary the modeled quantities at the inlet with varying f_k.

Third, there are the effects on the turbulent length scales l and L_{vk}, which appear in the second turbulence closure equation (Eq. (22)). One of the key features of the KSKL model is its inclusion of an additional length scale, the von Kármán length scale L_{vk}, given by Eq. (19), which, without the limiters, reduces to

$$L_{vk} = \frac{\kappa\langle S\rangle}{\sqrt{\frac{\partial^2\langle U_i\rangle}{\partial x_k^2}\frac{\partial^2\langle U_i\rangle}{\partial x_j^2}}} \tag{33}$$

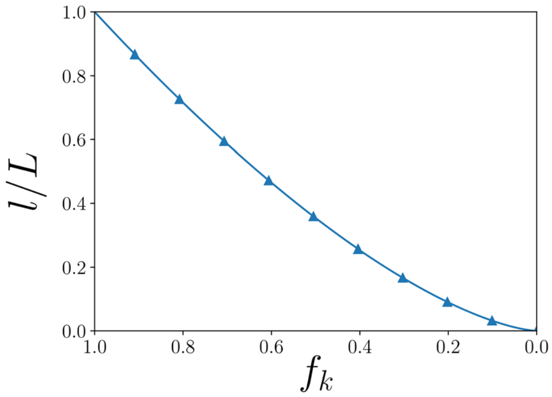

Fig. 2 Ratio l/L versus f_k according to Eq. (28) with $f_\varepsilon = 1.0$. Note the inversion of the horizontal axis, $f_k = 1.0$ on the left corresponds with RANS, $f_k = 0.0$ on the right corresponds with DNS.

The length scale is a function of the resolved strain rate $\langle S \rangle$ and the rate of change in the resolved acceleration $\partial^2 \langle U_i \rangle / x_j^2$. It is therefore solely based on the resolved velocity field. According to Ref. [49], who investigated different formulations for $L_{\nu K}$ in the context of scale-adaptive simulation, the von Kármán length scale can be considered as the second length scale in a RANS model for a fully developed planar turbulent boundary layer. This would erroneously imply that $L_{\nu K}$ should reduce together with f_k. Modification of f_k leads to differences in the strain rate and rate of change in acceleration, due to increased variations in the velocity field (as seen in Refs. [9] and [11]). A consequence is that $L_{\nu K}$ will increasingly vary in space and time with reducing f_k. However, the presumption in RANS is that the time-averaged velocity field—when all turbulence is modeled—is identical to the time-averaged velocity field when all turbulence is resolved. From this, it is expected that the time-averaged $L_{\nu K}$ is also independent of f_k.

This is not the case for the second length scale in the KSKL model, l, which is part of the convected secondary quantity $\sqrt{k}l$. By definition, this depends on f_k according to the relationship derived in Eq. (28), and is shown in Fig. 2. As expected, the ratio $l/L(-f_l)$ goes to zero with decreasing f_k, meaning that increasing the physical resolution leads to a RANS turbulent length scale going to zero, indicating that all turbulence should be resolved. It can also be shown that the slope of $\partial f_l / \partial f_k$ decreases when f_k approaches zero, implying an initially larger effect of reducing f_k, but less difference for lower f_k values. This is in line with results obtained with different ($k - \omega$ based) PANS closures [11,50].

4 Numerical Examples

The PANS-KSKL turbulence model is applied to two test cases and compared against the PANS-SST model. Following Ref. [50], $f_\varepsilon = 1.0$ to avoid excessive diffusion, and following Ref. [10], constant values of f_k are employed in time and space.

4.1 Turbulent Channel Flow at $\mathrm{Re}_\tau = 395$. The first test case is the canonical turbulent channel flow at $\mathrm{Re}_\tau = u_\tau \delta / \nu = 395$ in the setup as described in Ref. [11]. Here, u_τ indicates the wall friction velocity, U_b is the bulk velocity, and δ is the boundary layer thickness. Computations are performed using a rectangular domain, with two no-slip walls oriented normal to the y-axis, as shown in Fig. 3. The remaining boundaries are connected using periodic boundary conditions in order to approximate an infinite channel. The Cartesian grid density is $N_x = 127$, $N_y = 95$ and $N_z = 95$ with clustering toward the walls, resulting in $x^+ = u_\tau \Delta x / \nu \approx 12$, $y^+ = u_\tau \Delta y / \nu \approx 0.1$ and $z^+ = u_\tau \Delta z / \nu \approx 10$. Discretization errors were shown to be negligible in Ref. [11], making iterative errors more important for the total numerical error. The nondimensional time-step $\Delta t^* = u_\tau \Delta t / 2\delta \approx 1 \times 10^{-3}$ leads to $\Delta t^+ = u_\tau^2 \Delta t / \nu \approx 0.08$ or 2000 time steps per flow-through time. A body force is applied to maintain the proper Reynolds number. Time integration is performed using a second-order implicit scheme; the convection terms are discretized using a second-order accurate central differencing scheme (the Péclet number has a magnitude of $\mathcal{O}(10)$). The turbulence equations are discretized using a first-order upwind scheme. The results are compared against the DNS data by Ref. [51].

Figures 4 and 5 show the time-averaged (indicated by an overbar) mean velocity, turbulence kinetic energy spectra, eddy-viscosity ratio, turbulence intensity, and Reynolds stresses, for several f_k values. Next to the PANS-KSKL, PANS-SST results from Ref. [11] are also included. In line with the PANS-SST results, only low f_k values yield a resolved turbulent flow when using PANS-KSKL. For an explanation of this phenomenon, the reader is referred to Ref. [11]. The magnitude of the eddy viscosity predicted by PANS-KSKL is strongly reduced compared to PANS-SST, while the profiles are similar. For PANS-KSKL, the threshold to obtain a turbulent solution is $f_k = 0.25$, while for PANS-SST, the highest applicable f_k value was 0.15. This different threshold is a direct consequence of the reduced eddy-viscosity levels of the PANS-KSKL. As an example, for $f_k = 0.25$, ν_t/ν is almost 25 times higher for PANS-SST compared to PANS-KSKL, leading to dampening of the velocity fluctuations and a laminar flow solution. We know from literature that for SRS the effective computational Reynolds number

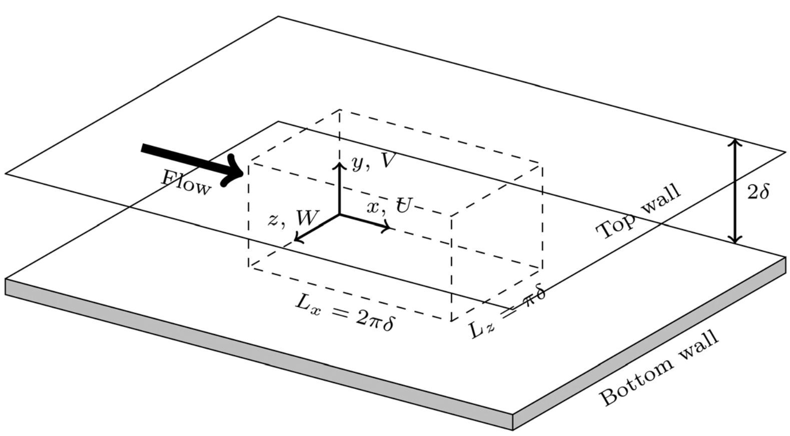

Symbol	Value
δ [m]	0.1
U_b [m/s]	6.928×10^{-2}
u_τ [m/s]	3.966×10^{-3}
τ_w [N/m^2]	1.570×10^{-1}
ν [m^2/s]	1.004×10^{-6}
Re_τ	3.95×10^2
Re_b	1.38×10^4

Fig. 3 Schematic overview of the domain and physical parameters. The dashed lines indicate the computational domain.

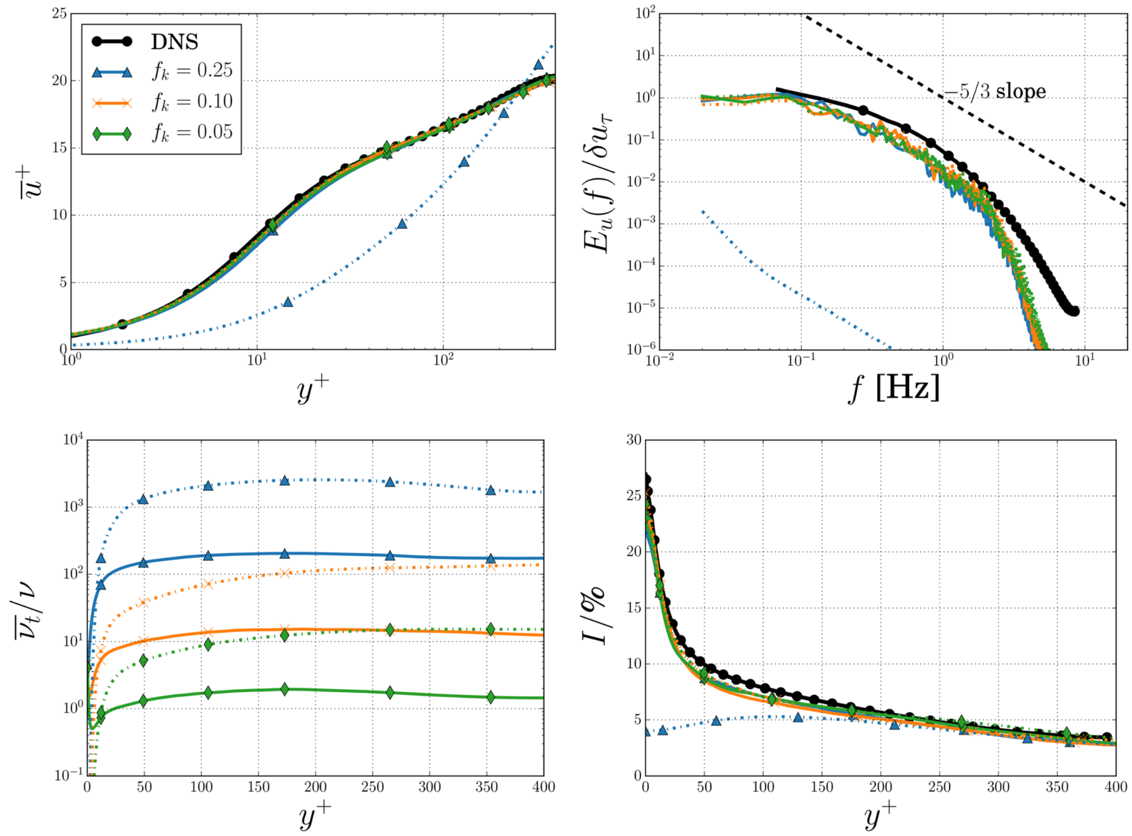

Fig. 4 Turbulent channel flow. Normalized mean velocity ($\overline{u}^+ = \overline{u}/u_\tau$), turbulence kinetic energy spectra ($E_u(f)$ at $y^+ \approx 20$), eddy-viscosity ratio (ν_t/ν) and turbulence intensity ($\mathcal{I} = \overline{u_i'}/U_b$), using PANS-KSKL (solid lines), PANS-SST (dashed lines) [11] and DNS [51]. From left to right, and top to bottom $\overline{u}^+$, $E_u(f)$ at $y^+ \approx 20$, ν_t/ν and $\mathcal{I}$.

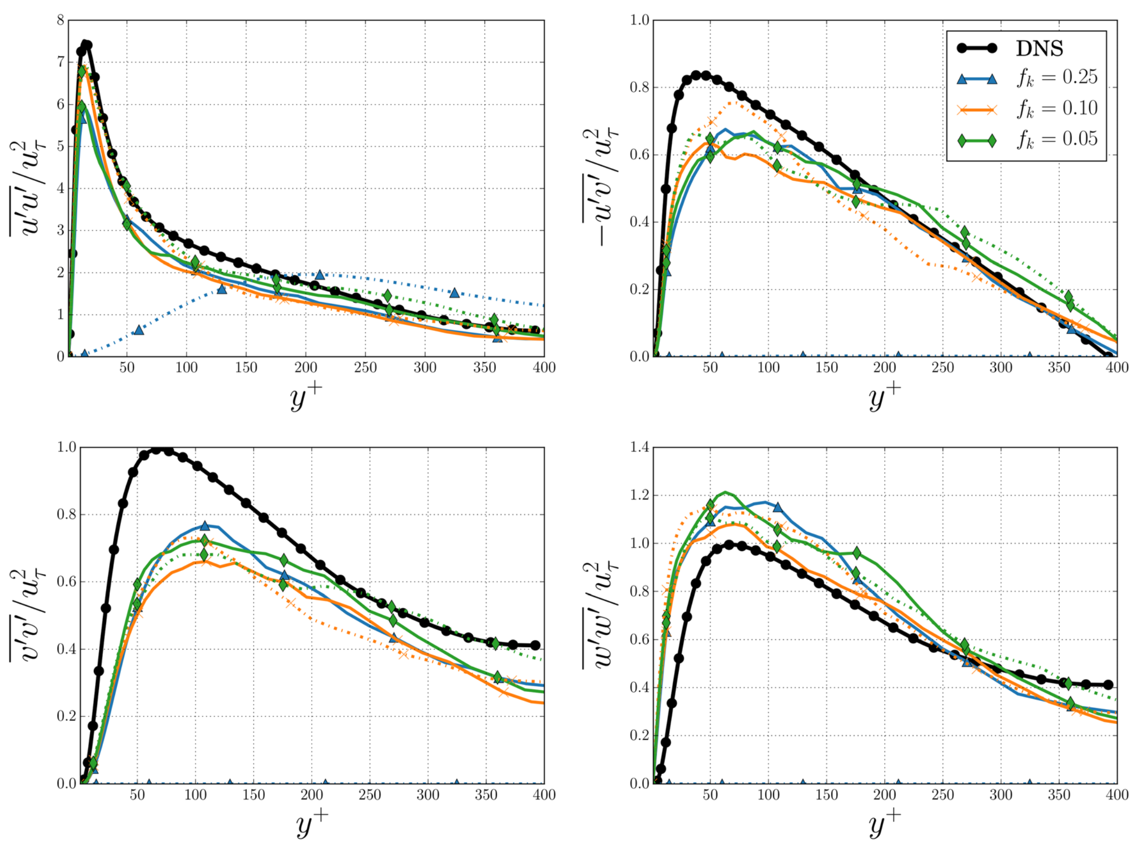

Fig. 5 Turbulent channel flow. Normalized Reynolds stress profiles ($\mathrm{Re}_{ij} = \overline{u_i'u_j'}/u_\tau^2$) using PANS-KSKL (solid lines), PANS-SST (dashed lines) [11] and DNS [51]. From left to right, and top to bottom Re_{uu}, Re_{uv}, Re_{vv}, and Re_{ww}.

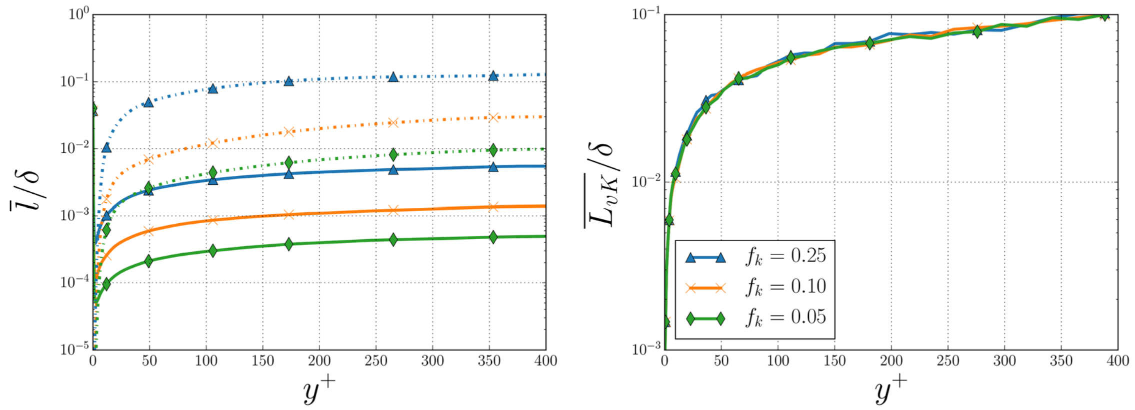

Fig. 6 Turbulent channel flow. Turbulence integral length scale (left) and von Kármán length scale (right) using PANS-KSKL (solid lines) and PANS-SST (dashed lines).

$$\mathrm{Re}_e = \frac{U\delta}{\nu + \nu_{\mathrm{modeled}}} = \frac{U\delta}{\nu + f_k^2 \nu_t} \tag{34}$$

must exceed the critical transition Reynolds number needed for the onset of instability, Re_c [11,52]. For a turbulent channel flow, $Re_c \approx 2300$, obtained from experiments [53]. When we equate the critical Reynolds number to the effective Reynolds number for both PANS models, we can derive the relationship

$$\frac{f_{k,\mathrm{SST}}}{f_{k,\mathrm{KSKL}}} = \sqrt{\frac{\nu_{t,\mathrm{KSKL}}}{\nu_{t,\mathrm{SST}}}} \tag{35}$$

From this relation, it is clear that the reduction in predicted eddy viscosity leads to a lower threshold for PANS-SST, compared to PANS-KSKL.

Figure 6 shows the modeled length scales and von Kármán length scale for several f_k values. For PANS-KSKL, the modeled length scale l is one order of magnitude smaller than for PANS-SST. In line with the explanations in Sec. 3.1, for the values of f_k which result in a resolved turbulent flow solution, L_{vK} is independent of f_k. $L_{vK}/\delta \approx 0.1$ in the center, and reduces toward the wall. For higher f_k values, for this test case, theoretically L_{vK} approaches infinity, since due to the steady, laminar, flow solution the denominator goes to zero. In practice, due to the inclusion of limiters, L_{vK} will be bound to $c_{l_2}\kappa d$, which is approximately 0.05 at the channel center, and decreases linearly to zero at the wall. This shows how the inclusion of L_{vK} allows "*the model to recognize and adjust to already resolved scales in the simulation*" [26]. This property is the foundation of scale-adaptive simulation, as investigated in detail by Ref. [49]. The effect mostly occurs in unsteady calculations exhibiting separation. This feature is retained when using the model as a subfilter model in PANS.

The different PANS closure strongly affects iterative convergence behavior. The convergence is assessed based on the residuals, which are normalized by the diagonal element of the left-hand-side matrix of the linear system of equations. To compare the convergence behavior the relaxation factors were kept constant: 0.2 for momentum, 0.2 for pressure, and 0.2 for the turbulence equations. Figure 7 shows the time-averaged convergence of all equations for the first 20 iterations per time-step, using $f_k = 0.1$, while Fig. 8 shows the effect of varying f_k on the convergence of the k and ω and $\sqrt{k}l$ equations. As expected, the convergence of the momentum, pressure and turbulence kinetic energy equations is hardly affected, but the residuals of the second turbulence equation vary significantly. The ω equation for PANS-SST with low f_k stagnates at $L_\infty \approx 10^{-2} - 10^{-3}$, with L_2 being two orders of magnitude lower. For PANS-KSKL, the $\sqrt{k}l$ equation both starts at a lower residual, as well as exhibiting a stronger decay. The equation reaches $L_\infty \approx 10^{-8}$, and is thereby the best converged equation. Using these settings, the wall clock time of a typical run time is approximately 5 days on 50 cores (Intel Xeon E5-2660 v3 CPU (10 core) at 2.60 GHz, with InfiniBand communication), this is independent of the choice for turbulence method.

Investigating the effect of f_k on the convergence of the turbulence equations (as shown in Fig. 8) indicates that reducing f_k (i.e., reducing the effect of the subfilter model) leads to reduced residuals, both for the k, and the ω and $\sqrt{k}l$ equations. The one exception is the ω equation for $f_k = 0.25$, which shows residuals four orders of magnitude lower than for $f_k = 0.10$ or 0.05. However, as seen in Figs. 4 and 5, this simulation predicts an incorrect laminar flow; hence, these low residuals are related to the unrepresentative flow field. As shown earlier, the residuals of the $\sqrt{k}l$ equation are on average five orders of magnitude lower than for the ω equation, and—with the exception of the $f_k = 0.05$ case—keep decreasing linearly with an increasing iteration number. These results confirm the expected behavior that a reduction of f_k (i.e., approaching DNS), leads to a reduction in iterative errors due to the subfilter turbulence model

4.2 Elliptical Wing. The second case is an elliptical wing with a NACA66_2-415 cross section, a root-chord of $c_0 = 0.1256$ m and a wingspan of $b = 0.15$ m, at $Re = U_\infty c_0/\nu = 8.95 \times 10^5$ where U_∞ is the freestream velocity. The wing is simulated in wetted and cavitating flow conditions (with a cavitation number $\sigma = (p_\infty - p_v)/(1/2\rho U_\infty^2) = 4.2$ and 1.7, respectively) where p_∞ is the farfield pressure and p_v the vapor pressure. The simulations are based on the setup of Ref. [29], but now use a synthetic inflow turbulence generator to prevent leading edge separation [47]. The computational domain corresponds to the cavitation tunnel of Delft University of Technology [54], with an inlet located $5c_0$ upstream of the wing and an outlet located $10c_0$ downstream. The domain is visualized in Fig. 9.

The boundary conditions at the inlet are a Dirichlet condition for all velocity components, with a RANS turbulence intensity of 1% and an eddy-viscosity ratio of 1.0. A Dirichlet condition for the pressure is prescribed at the outlet. The tunnel walls were modeled as slip walls, and the wing's surface as a no-slip wall. Turbulent fluctuations are added at $x/c_0 = -2.4$ using a body-forcing method, developed in Refs. [11] and [47], based on the digital filtering method by Ref. [55]. Homogeneous isotropic turbulence is prescribed, resulting in a turbulence intensity at the location of the wing tip of $\mathcal{I}_{tip} \approx 2.0\%$, with an integral length scale of $\ell/c_0 = 0.8$ ($\ell/r_c \approx 100$ with r_c being the cavity radius).

A multiblock hexahedral structured grid is used, with additional refinement around the wing's edges. To minimize numerical diffusion, a priori grid refinement was employed to increase the resolution in the vortex and wake regions [56]. For the resolution in the vortex, the recommendation by Ref. [57] of an in-plane and

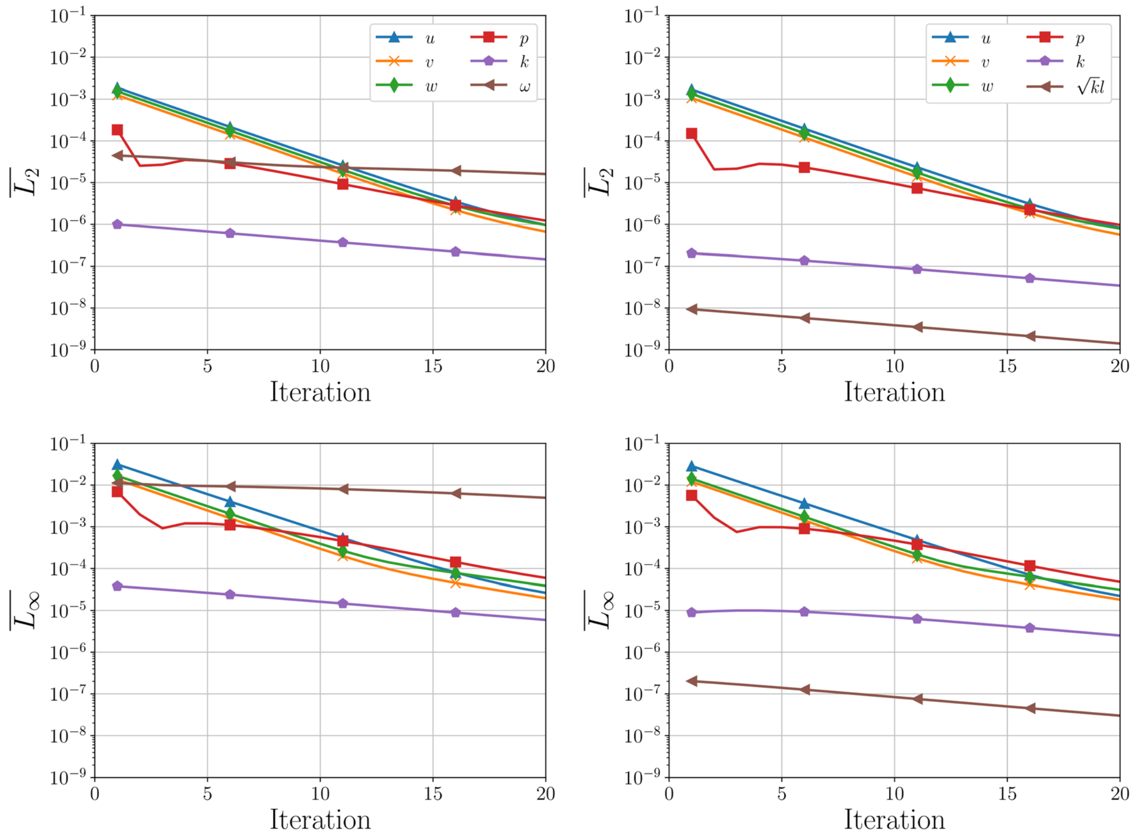

Fig. 7 Turbulent channel flow. Time-averaged iterative convergence for the different equations, using PANS-SST (left) and PANS-KSKL (right) with $f_k = 0.1$.

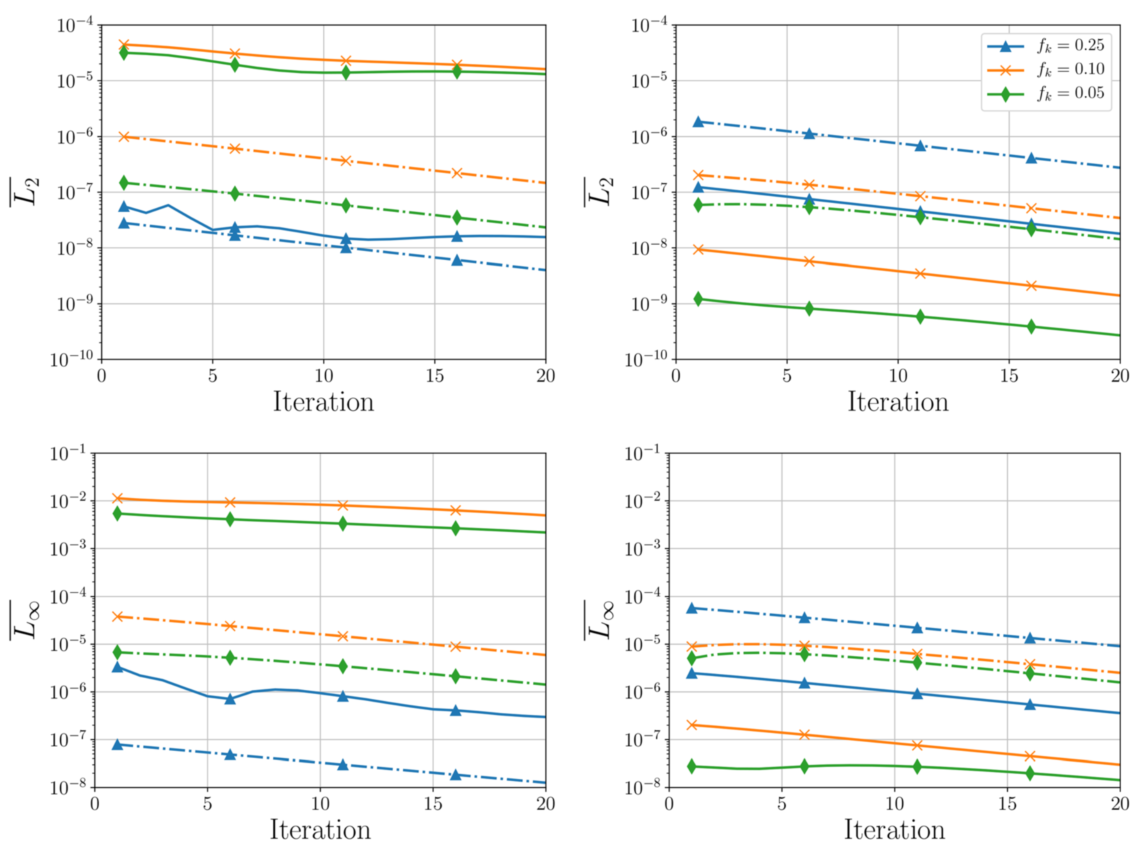

Fig. 8 Turbulent channel flow. Time-averaged iterative convergence for k (dashed lines), and ω and $\sqrt{k}l$ (solid lines) equations, using PANS-SST (left) and PANS-KSKL (right) for varying f_k.

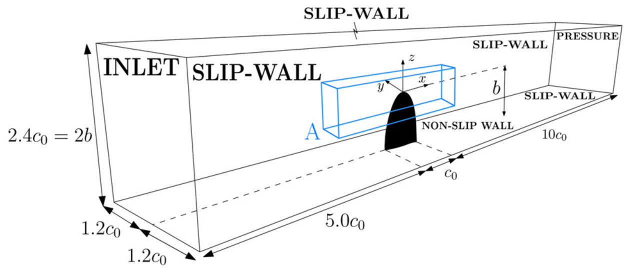

Fig. 9 Schematic visualization of computational domain including geometrical parameters expressed in c_0, and boundary conditions. Adapted from Ref. [29].

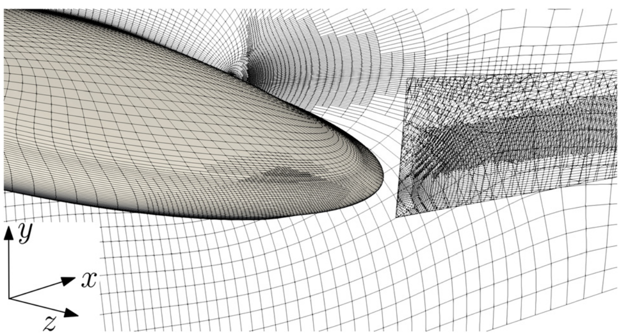

Fig. 10 Elliptical wing. Visualization of the wing surface grid, the wake region, and the vortex region indicated by box A in Fig. 9. Adapted from Ref. [29].

streamwise resolution of $r_v/8$ and $r_v/4$ was met for the finest grid, with r_v the viscous core radius. Upstream of the wing, between the turbulence generator and the wing, an additional refinement box is located. The grid consists of 7.44×10^6 cells. At the wing surface, the surface averaged, nondimensional cell sizes are $\overline{x_n^+} = 0.1$, $\overline{x_t^+} = 160$ and $\overline{x_s^+} = 330$ in normal (n), tangential (t), and spanwise (s) directions, respectively. The grid is visualized in Fig. 10. The nondimensional time-step $\Delta t^* = U_\infty \Delta t / c_0 \approx 1 \times 10^{-2}$. The convective terms are discretized with the second-order accurate limited quadratic upwind interpolation for convective kinematics (QUICK) scheme, while for turbulence and cavitation equations a first-order upwind scheme was used. Simulations are performed with a fixed $f_k = 0.1$. For the mass transfer model, the number of seeds was set to 1×10^9 m^{-3} and the bubble radius to 3×10^{-5} m [29]. The wall clock time of a typical run time is approximately 7 days on 200 cores (Intel Xeon E5-2660 v3 CPU (10 core) at 2.60 GHz, with InfiniBand communication), this is again independent of the choice for turbulence method.

The time-averaged obtained residuals for PANS-KSKL and PANS-SST for the momentum (u, v, w), pressure (p), vapor volume fraction (α_v), and turbulence equations are shown in Fig. 11. The relaxation factors were 0.25 for momentum, 0.10 for pressure, 0.25 for turbulence, and 0.25 for the cavitation equation. The convergence for PANS-SST and PANS-KSKL is similar for momentum, pressure, and vapor volume fraction. For PANS-KSKL, the convergence of the turbulence kinetic energy equation is slightly reduced compared to PANS-SST, which has been observed before in the context of RANS predictions for propellers [58], and is likely related to the reduced eddy viscosity. A reduction in eddy viscosity reduces diffusion (see Eq. (17)), thereby making the transport equation for k more difficult to solve. The main difference, however, occurs again for the second turbulence equation. For PANS-SST, the ω equation stagnates at $\overline{L_2} = 10^{-3}$ with $\overline{L_\infty} = 10^1$. This is a common occurrence for $k-\omega$ models in

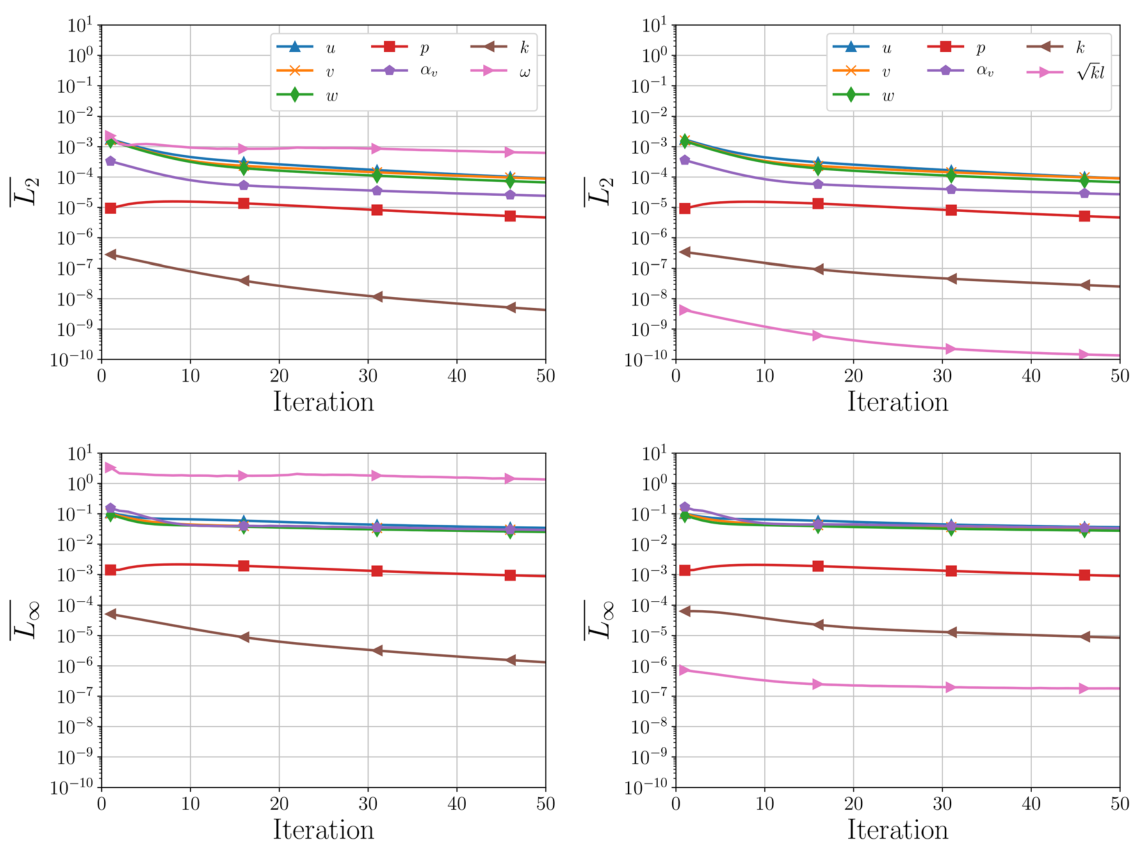

Fig. 11 Elliptical wing. Time-averaged iterative convergence for the different equations, using PANS-SST (left) and PANS-KSKL (right) with $f_k = 0.1$.

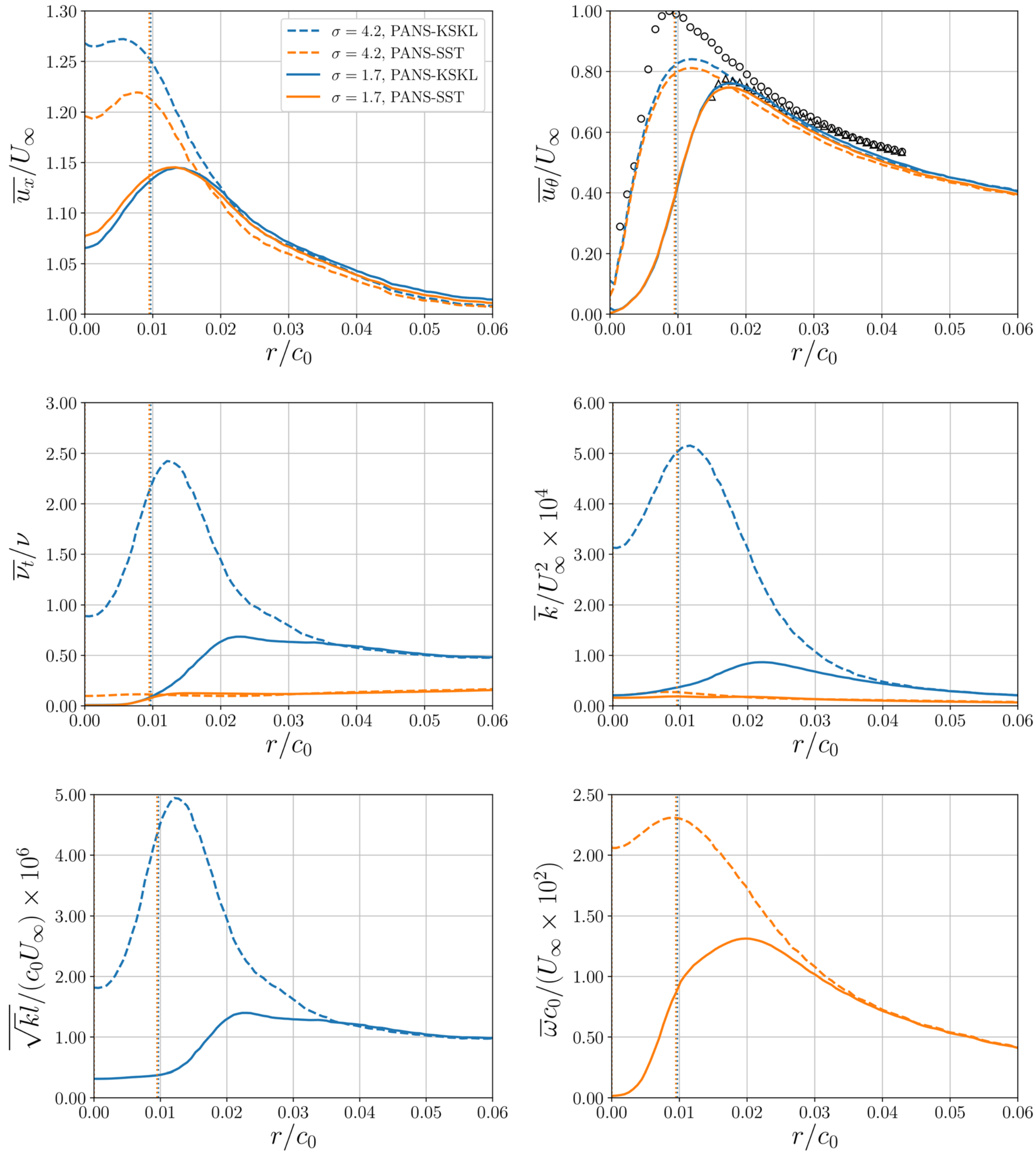

Fig. 12 Elliptical wing. Radial distribution of time-averaged axial and azimuthal velocity, eddy-viscosity ratio, turbulence kinetic energy, and second turbulence variable at $x/c_0 = 0.5$ downstream of the wing tip. Dashed lines indicate wetted flow, and solid lines indicate cavitating flow. Vertical dotted lines correspond to the cavity radius r_c. Experimental data adapted from Ref. [54].

conjunction with cavitation modeling (see, e.g., Refs. [29] and [47]). In contrast, the $\sqrt{k}l$ equation continues to converge, and within 50 iterations reaches $\overline{L_2} = 10^{-10}$, even when used in combination with the vapor volume fraction transport equation. This demonstrates that the superior convergence behavior of the KSKL closure is maintained in multiphase flow conditions.

The predicted kinematics of the cavitating tip vortex are analyzed at $x/c_0 = 0.5$ downstream of the wing tip. Figure 12 shows the time- and circumferential-averaged profiles of axial $(\overline{u_x}/U_\infty)$ and azimuthal velocity $(\overline{u_\theta}/U_\infty)$, eddy-viscosity ratio $(\overline{\nu_t}/\nu)$, normalized modeled turbulence kinetic energy $(\overline{k}/U_\infty^2)$ and normalized second turbulence variable along the radius. Only the azimuthal velocity is compared to data obtained using PIV [54]. The vapor volume fraction and pressure coefficient $(\overline{C_p} = (\overline{p} - p_\infty)/(1/2\rho U_\infty^2))$ are given in Fig. 13. The time-averaged normalized cavity radius (defined based on a vapor volume fraction $\alpha_v = 0.1$) is $r_c/c_0 \approx 0.01$ for both PANS closures.

In wetted flow conditions the PANS-KSKL model predicts a higher axial velocity at the viscous core radius than the PANS-SST model. Both models show a reduction in axial velocity at the vortex core $(r/c_0 \leq 0.05)$, which is an indication of increased physics in the simulation. Evidence for this behavior can be observed in the experimental results reported by Ref. [59]. The increase in axial velocity toward in the region $r/c_0 \leq 0.02$ is also an improvement compared to the wetted flow results obtained using delayed detached eddy simulation (DDES) and improved delayed detached eddy simulation (IDDES), reported by Ref. [29]. For those results $\max(\overline{u_x}/U_\infty) \approx 1.1$, which is a significant underprediction compared to the experimentally observed values. The maximum azimuthal velocity is underpredicted by 20% by both PANS models. In cavitating conditions, the predicted viscous core radii $(r_v = \mathrm{argmax}(u_\theta))$ and azimuthal velocity magnitudes match the experimental values. The inclusion of cavitation reduces the axial velocity at the

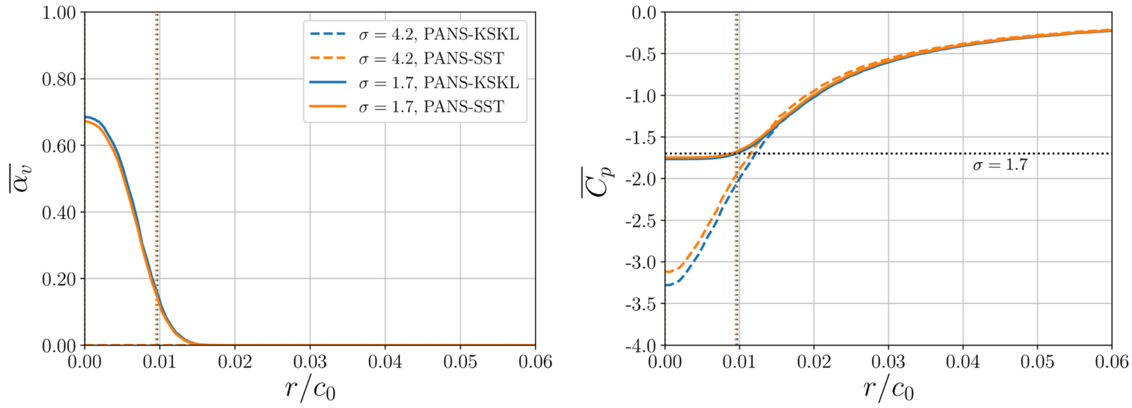

Fig. 13 Elliptical wing. Radial distribution of vapor volume fraction and pressure coefficient at $x/c_0 = 0.5$ downstream of the wing tip. Dashed lines indicate wetted flow, and solid lines indicate cavitating flow. Vertical dotted lines correspond to the cavity radius r_c.

vortex core and increases the viscous core radius, compared to wetted flow.

As expected, the eddy-viscosity levels for $f_k = 0.1$ are orders of magnitude lower than for a full RANS ($f_k = 1.0$) solution (not shown in this work). The inclusion of cavitation reduces the eddy viscosity to zero inside the cavity radius. In line with the expectations formulated in Sec. 3.2, the eddy viscosity in the farfield predicted by PANS-KSKL—for this f_k—is approximately three times larger than the eddy viscosity produced by PANS-SST. In wetted flow conditions, the PANS-KSKL eddy viscosity also shows a large peak at the viscous core radius, which is absent for PANS-SST. Technically, the assumptions of a uniform, steady flow, made in the derivation of eddy-viscosity decay, are not valid in this case, due to the inclusion of synthetic inflow turbulence. Despite this, it does explain the higher ν_t/ν in the farfield. The effect of varying f_k on the eddy-viscosity decay is outside of the scope of this work, but was investigated in Ref. [47] for PANS-SST. It is important to note that for cavitating conditions, at the cavity radius, the eddy-viscosity ratios are similar in magnitude, implying similar cavitation dynamics. Compared to PANS-SST, higher levels of k are observed for PANS-KSKL. The peak in k coincides with the peak in ν_t/ν and is just outside the viscous core radius.

Comparing the values for the second turbulence variable, obtained by two different turbulence closures, is not straightforward, due to the different formulations. For both models, the inclusion of cavitation reduces the magnitude in the region $r/c_0 \leq 0.03$. In line with expectations, PANS-SST predicts high

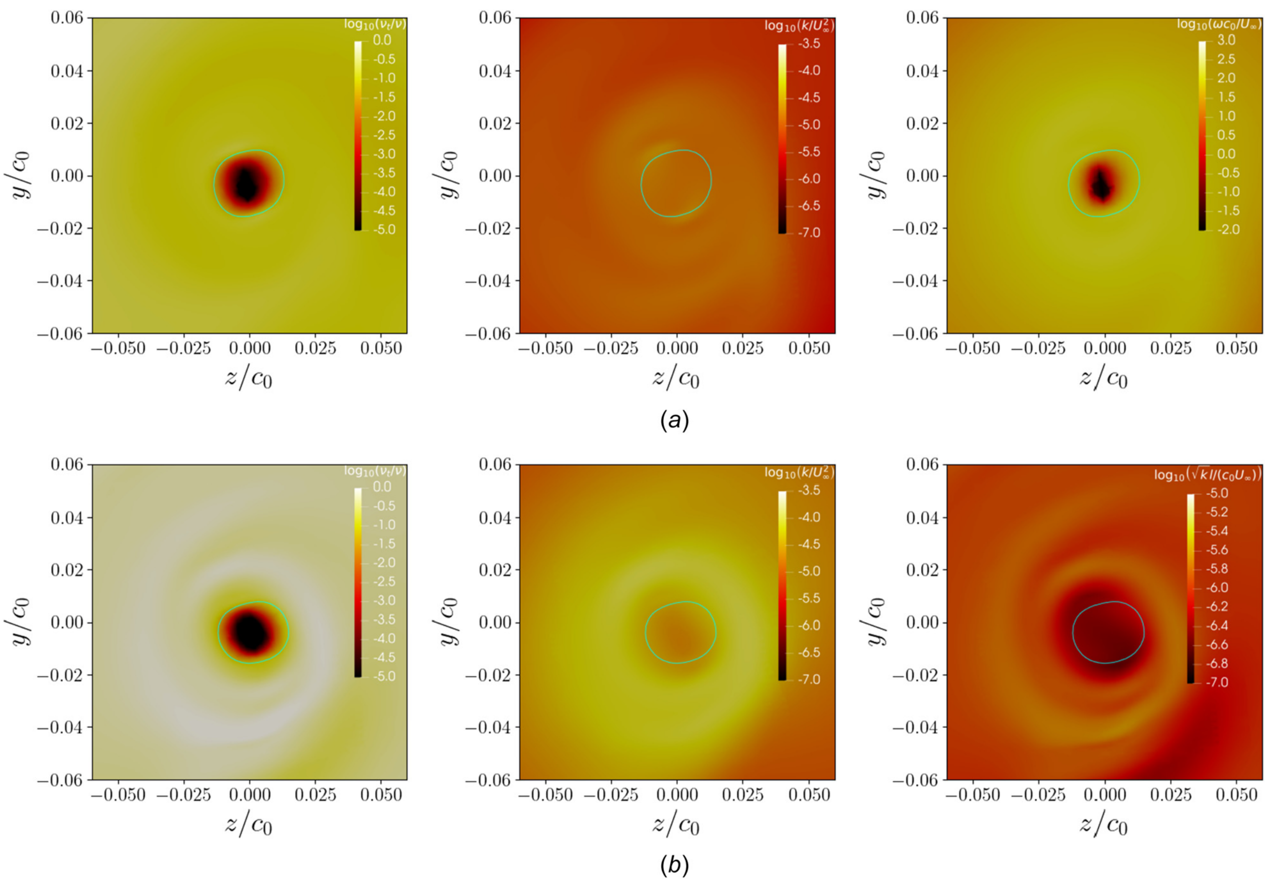

Fig. 14 Elliptical wing. Instantaneous ν_t/ν, k and $\sqrt{k}l$ or ω, for PANS-SST and PANS-KSKL, at $x/c_0 = 0.5$ downstream of the wing tip in cavitating conditions ($\sigma = 1.7$). The cavity radius, $\alpha_v = 0.1$, is indicated in cyan ($r_c/c_0 \approx 0.01$).

diffusion in the entire field (with the exception of the vortex core). From RANS modeling it is known that the SST model performs poorly in strongly rotating flows, leading to the use of curvature corrections, see, e.g., Ref. [57]. In contrast, in cavitating conditions, PANS-KSKL shows a constant, low, diffusion inside the cavity radius, with a peak at a higher radius compared to PANS-SST. In wetted flow conditions, there is a large difference in $\sqrt{k}l$ between the vortex core and viscous core radius. This reduction outside the vortex core also occurs for PANS-SST, but the difference in magnitude is significantly smaller, again highlighting the difficulties of applying the SST model for rotational flows.

The PANS-KSKL model predicts a lower pressure coefficient in the vortex core in wetted flow conditions, compared to PANS-SST. This is related to the increased axial velocity. In cavitating conditions, both models show identical pressure profiles, but the vapor volume fraction is slightly higher for the PANS-KSKL model.

Figure 14 shows—for cavitating conditions—the distribution of the instantaneous normalized eddy viscosity, modeled turbulence kinetic energy and second turbulence values at the same location as Fig. 12. The distribution of $\sqrt{k}l$ clearly shows the roll-up process of the vortex. These differences in the second turbulence variables also contribute to the differences in eddy viscosities. For PANS-KSKL, the eddy viscosity is defined as the minimum of two terms, $C_\mu^{1/4}\sqrt{k}l$ and $a_1 k/\langle S\rangle$ (see Eq. (15)). Inside the cavity radius, ν_t is defined by term II, due to the high strain rate caused by the rotation, while outside of this radius, it is determined by term I. This can be seen by comparing the distributions of ν_t/ν and $\sqrt{k}l$ in Fig. 14. In contrast, for PANS-SST, the eddy viscosity is given by

$$\nu_t = \frac{a_1 k}{\max(a_1\omega, \langle S\rangle F_2)} \tag{36}$$

As for PANS-KSKL, at the vortex core, ν_t is defined by the second term in the max function, due to the high strain rate caused by the rotation. Further outwards the dissipation rate dominates. The high diffusion rate around the vortex leads to a lower eddy viscosity.

From these definitions, it is easily observed that the limiters depend on the used f_k value. When we express the eddy viscosity in the RANS turbulence kinetic energy length scale and dissipation rate, we obtain

$$\nu_t = \min\left(C_\mu^{1/4}\frac{f_k^2}{f_\varepsilon}\sqrt{K}L; \frac{a_1 f_k K}{\langle S\rangle}\right) \tag{37}$$

for PANS-KSKL, and

$$\nu_t = \frac{a_1 f_k K}{\max\left(a_1\dfrac{f_\varepsilon \Omega}{f_k}, \langle S\rangle F_2\right)} \tag{38}$$

for PANS-SST. Both of the limiters in these functions show a similar trend: with decreasing f_k, the region depending on term II (depending on the strain rate) decreases in size, while the eddy viscosity in a larger part of the domain is depends on either $\sqrt{k}l$ or ω. Interestingly, the trends are not identical. For PANS-KSKL term I decreases quadratically, and term II linearly; for PANS-SST however, term I decreases linearly, and term II is independent on f_k. This partly explains why the secondary turbulence transport equation for PANS-KSKL (with lower f_k values) is better suited for rotational flows than the ω equation, since the ω equation requires more arbitrary limiting.

5 Conclusions

A new PANS closure has been derived based on the KSKL model. Simulations using low f_k values show that the favorable properties of decreased eddy viscosity and improved iterative convergence exhibited by the KSKL model compared to $k-\omega$ models are carried over to the PANS model. It is shown that the improvement in iterative convergence holds for multiphase flows, for which the ω equation is well known for being difficult to converge, making this model suitable for cases such as simulating cavitation dynamics and underwater radiated noise. In common engineering practice, higher f_k values than those values used in this work might be more typical, although the benefits demonstrated here are expected to be maintained, since they largely derive from the parent RANS model. It was also shown—theoretically and numerically—that the PANS-KSKL model exhibits a low decay of eddy viscosity downstream of the inlet boundary condition for $f_k < 1.0$, potentially simplifying practical application compared to the PANS-SST model. The influence of f_k on the auxiliary functions, and the decay of the eddy viscosity prescribed at the inlet—and the effect this has on the results—requires further numerical investigation.

Acknowledgment

The simulations were carried out on the *Reynolds* (Delft University of Technology) and *Marclus4* (MARIN) clusters. The authors acknowledge Rui Lopes (IST Lisbon) for his assistance with deriving the SST and KSKL eddy-viscosity decay functions.

Funding Data

- Dutch Research Council (Nederlandse Organisatie voor Wetenschappelijk Onderzoek), as part of the NOISOURCE project (ALWTW.2016.008; Funder ID: 10.13039/501100003246).

Nomenclature

b = wing span (m)
c_0 = wing root chord length (m)
C_p = pressure coefficient
d = near wall distance (m)
D = destruction term
$E_u(f)$ = power spectral density of u velocity component (m^2/s)
f_k = ratio of modeled-to-total turbulence kinetic energy
$f_{\sqrt{k}l}$ = ratio of modeled-to-total $\sqrt{k}l$
f_l = ratio of modeled-to-total turbulence integral length scale
f_ε = ratio of modeled-to-total turbulence dissipation
f_ω = ratio of modeled-to-total turbulence dissipation rate
I = turbulence intensity
k, K = turbulence kinetic energy (m^2/s^2)
l = liquid
ℓ = integral turbulence length scale at inflow boundary condition
l, L = turbulence integral length scale (m)
L_x, L_y, L_z = domain length (m)
L_{vK} = von Kármán length scale (m)
$L_2,\ L_\infty$ = residual norms
$\dot{m}$ = cavitation source term (kg/(m^{3}s))
N = number of cells
P = static pressure (Pa)
P = production term
r = radius (m)
r_c = cavity core radius (m)
r_v = viscous core radius (m)
Re = Reynolds number
Re$_b$ = wall friction Reynolds number
Re$_c$ = critical transition Reynolds number
Re$_e$ = effective computational Reynolds number
Re$_\tau$ = wall friction Reynolds number
Re$_{ij}$ = resolved Reynolds stress components (m^2/s^2)

S = magnitude of strain rate tensor (1/s)
S_{ij} = strain rate tensor (1/s)
T = time (s)
u_x = axial velocity component (m/s)
u_θ = azimuthal velocity component (m/s)
u_τ = wall friction velocity (m/s)
U_b = bulk velocity (m/s)
U_i = velocity components (U,V,W) (m/s)
v = vapor
V = phase volume (m^3)
x_i = spatial coordinates (x,y,z) (m)
x^+, y^+, z^+ = non-dimensional cell sizes
y = cell height (m)
α = volume fraction
δ = boundary layer thickness (m)
δ_{ij} = Kronecker delta
Δt = timestep (s)
Δt^*, Δt^+ = non-dimensional timestep
Δx, Δy, Δz = cell sizes (m)
ε, E = turbulence dissipation (m^2/s^2)
ϕ = modeled component of Φ
Φ = arbitrary quantitiy of Φ
$\langle\Phi\rangle$ = resolved component of Φ
κ = von Kármán constant
μ = dynamic viscosity (kg/(ms))
ν = kinematic viscosity (m^2/s)
ν_t = eddy viscosity (m^2/s)
ρ = density (kg/m^3)
σ = cavitation number
τ_{ij} = modeled Reynolds stress tensor (m^2/s^2)
τ_w = skin friction (N/m^2)
ω, Ω = turbulence dissipation rate (1/s)
∞ = value at farfield

Appendix A: Eddy-Viscosity Decay Derivations

A.1 Partially Averaged Navier–Stokes-Shear Stress Transport

The PANS-SST equations are

$$\frac{\partial k}{\partial t}+\frac{\partial}{\partial x_j}\cdot\left(k\langle U_j\rangle\right)=P_k-\beta^*\omega k+\frac{\partial}{\partial x_j}\left[\left(\nu+\nu_t\sigma_k\frac{f_\omega}{f_k}\right)\frac{\partial k}{\partial x_j}\right] \tag{A1}$$

and

$$\begin{aligned}\frac{\partial \omega}{\partial t}+\frac{\partial}{\partial x_j}\cdot\left(\omega\langle U_j\rangle\right)&=\frac{\alpha}{\nu_t}P_k-\left(P'-\frac{P'}{f_\omega}+\frac{\beta\omega}{f_\omega}\right)\omega\\&\quad+\frac{\partial}{\partial x_j}\left[\left(\nu+\nu_t\sigma_\omega\frac{f_\omega}{f_k}\right)\frac{\partial \omega}{\partial x_j}\right]\\&\quad+2\frac{\sigma_{\omega 2}f_\omega}{\omega\ f_k}(1-F_1)\frac{\partial k}{\partial x_j}\frac{\partial \omega}{\partial x_j}\end{aligned} \tag{A2}$$

with

$$P'=\frac{\alpha\beta^* k}{\nu_t} \tag{A3}$$

When we assume a steady, uniform flow aligned with the x-axis, sufficiently far away from walls and neglecting the diffusion terms, with $\nu_t=k/\omega$, the equations simplify to

$$\langle U\rangle\frac{\mathrm{d}k}{\mathrm{d}x}=-\beta^*\frac{k^2}{\nu_t} \tag{A4}$$

and

$$\langle U\rangle\frac{\mathrm{d}\omega}{\mathrm{d}x}=-\left(P'-\frac{P'}{f_\omega}+\frac{\beta\omega}{f_\omega}\right)\omega \tag{A5}$$

Inserting Eq. (A3), and using the common assumption of $f_\varepsilon=1.0$, this reduces to

$$\langle U\rangle\frac{\mathrm{d}\omega}{\mathrm{d}x}=-(\alpha\beta^*-\alpha\beta^*f_k+\beta f_k)\omega^2 \tag{A6}$$

This equation can be solved by rewriting and integrating, to obtain the solution

$$\omega=\frac{\langle U\rangle\omega_{\mathrm{in}}}{\langle U\rangle+(\alpha\beta^*-\alpha\beta^*f_k+\beta f_k)(x-x_{\mathrm{in}})\omega_{\mathrm{in}}} \tag{A7}$$

Here, the subscript *in* indicates values at the inlet of the domain. Using this solution, we can solve Eq. (A4) by integrating, to obtain the solution

$$k=\frac{k_{\mathrm{in}}}{\left[\frac{1}{\langle U\rangle}\left(\langle U\rangle+(\alpha\beta^*-\alpha\beta^*f_k+\beta f_k)(x-x_{\mathrm{in}})\frac{k_{\mathrm{in}}}{\nu_{t,\mathrm{in}}}\right)\right]^{\frac{\beta^*}{\alpha\beta^*-\alpha\beta^*f_k+\beta f_k}}} \tag{A8}$$

To derive a transport equation for the eddy-viscosity, we can use the definition

$$\begin{aligned}\langle U\rangle\frac{\mathrm{d}\nu_t}{\mathrm{d}x}&=\langle U\rangle\frac{\mathrm{d}(k\omega^{-1})}{\mathrm{d}x_j}\\&=\frac{1}{\omega^2}\left(\omega\langle U\rangle\frac{\mathrm{d}k}{\mathrm{d}x}-k\langle U\rangle\frac{\mathrm{d}\omega}{\mathrm{d}x}\right)\end{aligned} \tag{A9}$$

Inserting Eqs. (A4) and (A6), yields

$$\langle U\rangle\frac{\mathrm{d}\nu_t}{\mathrm{d}x}=-(\beta^*-\alpha\beta^*+\alpha\beta^*f_k-\beta f_k)k \tag{A10}$$

We can obtain a solution for this equation, again using the definition of $\nu_t=k/\omega$, and the solutions for the decay functions of k and ω, see Eqs. (A7) and (A8)

$$\nu_t=\frac{\nu_{t,\mathrm{in}}}{\left[\frac{1}{\langle U\rangle}\left(\langle U\rangle+(\alpha\beta^*-\alpha\beta^*f_k+\beta f_k)(x-x_{\mathrm{in}})\frac{k_{\mathrm{in}}}{\nu_{t,\mathrm{in}}}\right)\right]^{\frac{\beta^*}{\alpha\beta^*-\alpha\beta^*f_k+\beta f_k}-1}} \tag{A11}$$

A.2 Partially Averaged Navier–Stokes k–$\sqrt{k}L$

The PANS-KSKL equations are

$$\frac{\partial k}{\partial t}+\frac{\partial}{\partial x_j}\cdot\left(k\langle U_j\rangle\right)=P_k-D_k+\frac{\partial}{\partial x_j}\left[\left(\nu+\frac{\nu_t}{\sigma_k\sqrt{f_k f_l}}\right)\frac{\partial k}{\partial x_j}\right] \tag{A12}$$

and

$$\frac{\partial(\sqrt{k}l)}{\partial t}+\frac{\partial}{\partial x_j}\cdot\left(\sqrt{k}l\langle U_j\rangle\right)=\frac{\sqrt{k}l}{\sqrt{f_k}f_l k}\nu_t\langle S\rangle^2\left(\zeta_1-\zeta_2\left(\frac{l}{f_l L_{vk}}\right)^2\right)-\zeta_3 k\frac{f_l}{\sqrt{f_k}}+\frac{\partial}{\partial x_j}\left[\left(\nu+\frac{\nu_t}{\sigma_{\sqrt{k}l}\sqrt{f_k}f_l}\right)\frac{\partial(\sqrt{k}l)}{\partial x_j}\right]-6\nu\frac{\sqrt{k}l}{\sqrt{f_k}f_l d^2}F_{\sqrt{k}l} \tag{A13}$$

Again, under the assumption of a steady, uniform flow aligned with the x-axis, sufficiently far away from walls, with neglecting the diffusion terms, the equations simplify to

$$\langle U\rangle\frac{\mathrm{d}k}{\mathrm{d}x}=-C_\mu^{3/4}\frac{k^{3/2}}{l} \tag{A14}$$

and

$$\langle U\rangle\frac{\mathrm{d}(\sqrt{k}l)}{\mathrm{d}x}=-\zeta_3 k\frac{f_l}{\sqrt{f_k}} \tag{A15}$$

These equations have no simple solution; hence, we consider a transport equation for the eddy-viscosity. When assuming uniform flow, the eddy-viscosity is given by

$$\nu_t=C_\mu^{1/4}\sqrt{k}l \tag{A16}$$

Using this, and the assumption of $f_\varepsilon=1.0$, we can rewrite Eqs. (A14) and (A15) to

$$\langle U\rangle\frac{\mathrm{d}k}{\mathrm{d}x}=-C_\mu\frac{k^2}{\nu_t} \tag{A17}$$

and

$$\langle U\rangle\frac{\mathrm{d}(\nu_t)}{\mathrm{d}x}=-(\beta^*-\beta_{\mathrm{KSKL}})k \tag{A18}$$

with the additional constant β_{KSKL} such that

$$\zeta_3 C_\mu^{1/4}f_k=\beta^*-\beta_{\mathrm{KSKL}} \tag{A19}$$

While the functions Eqs. (A17) and (A18) are not easily solved, it is important to realize the similarity with the decay functions of the PANS-SST model (Eqs. (A4) and (A10), respectively). The functions are identical, except for the constants, implying solutions of a similar form. Consequently, based on Eq. (A8), the decay of k is given by

$$k=\frac{k_{\mathrm{in}}}{\left[\frac{1}{\langle U\rangle}\left(\langle U\rangle+\beta_{\mathrm{KSKL}}(x-x_{\mathrm{in}})\frac{k_{\mathrm{in}}}{\nu_{t,\mathrm{in}}}\right)\right]^{\frac{\beta^*}{\beta_{\mathrm{KSKL}}}}} \tag{A20}$$

and, based on Eq. (A11), the decay of ν_t is given by

$$\nu_t=\frac{\nu_{t,\mathrm{in}}}{\left[\frac{1}{\langle U\rangle}\left(\langle U\rangle+\beta_{\mathrm{KSKL}}(x-x_{\mathrm{in}})\frac{k_{\mathrm{in}}}{\nu_{t,\mathrm{in}}}\right)\right]^{\frac{\beta^*}{\beta_{\mathrm{KSKL}}}-1}} \tag{A21}$$

References

[1] Nallasamy, M., 1987, "Turbulence Models and Their Applications to the Prediction of Internal Flows: A Review," Comput. Fluids, **15**(2), pp. 151–194.
[2] Pope, S., 2000, *Turbulent Flows*, Cambridge University Press, London.
[3] Argyropoulos, C., and Markatos, N., 2015, "Recent Advances on the Numerical Modelling of Turbulent Flows," Appl. Math. Modell., **39**(2), pp. 693–732.
[4] Pereira, F., Eça, L., Vaz, G., and Girimaji, S., 2021, "Toward Predictive RANS and SRS Computations of Turbulent External Flows of Practical Interest," Arch. Comput. Methods Eng., **28**(5), pp. 3953–4029.
[5] Smagorinsky, J., 1963, "General Circulation Experiments With the Primitive Equations: I. The Basic Experiment," Mon. Weather Rev., **91**(3), pp. 99–164.
[6] Spalart, P., 1997, "Comments on the Feasibility of LES for Wings, and on a Hybrid RANS/LES Approach," Proceedings of 1st AFOSR International Conference on DNS/LES, Ruston, LO, Aug. 4–8, Greyden Press, pp. 1–11.
[7] Girimaji, S., and Abdol-Hamid, K., 2005, "Partially Averaged Navier-Stokes Model for Turbulence: Implementation and Validation," AIAA Paper No. 2005-502.
[8] Girimaji, S., 2006, "Partially-Averaged Navier-Stokes Model for Turbulence: A Reynolds-Averaged Navier-Stokes to Direct Numerical Simulation Bridging Method," ASME J. Appl. Mech., **73**(3), pp. 413–421.
[9] Pereira, F., Vaz, G., Eça, L., and Girimaji, S., 2018, "Simulation of the Flow Around a Circular Cylinder at Re = 3900 With Partially-Averaged Navier-Stokes Equations," Int. J. Heat Fluid Flow, **69**, pp. 234–246.
[10] Klapwijk, M., Lloyd, T., and Vaz, G., 2019, "On the Accuracy of Partially Averaged Navier-Stokes Resolution Estimates," Int. J. Heat Fluid Flow, **80**, p. 108484.
[11] Klapwijk, M., Lloyd, T., Vaz, G., and Van Terwisga, T., 2020, "Evaluation of Scale-Resolving Simulations for a Turbulent Channel Flow," Comput. Fluids, **209**, p. 104636.
[12] Abdol-Hamid, K., and Girimaji, S., 2004, "A Two-Stage Procedure Toward the Efficient Implementation of PANS and Other Hybrid Turbulence Models," NASA Langley Research Center, Hampton, VA, Technical Memorandum.
[13] Basu, D., Hamed, A., and Das, K., 2007, "Assessment of Partially Averaged Navier Stokes (PANS) Multiscale Model in Transonic Turbulent Separated Flows," ASME Paper No. FEDSM2007-37630.
[14] Basara, B., Krajnovic, S., and Girimaji, S., 2008, "PANS vs. LES for Computations of the Flow Around a 3D Bluff Body," Proceedings of 7th International Symposium on Engineering, Turbulence, Modelling and Measurements, Vol. 2, Limassol, Cyprus, June 4–6, p. 3.
[15] Jeong, E., and Girimaji, S., 2010, "Partially Averaged Navier-Stokes (PANS) Method for Turbulence Simulations—Flow Past a Square Cylinder," ASME J. Fluids Eng., **132**(12), p. 121203.
[16] Davidson, L., and Friess, C., 2019, "A New Formulation of f_k for the PANS Model," J. Turbul., **20**(5), pp. 322–336.
[17] Friess, C., and Davidson, L., 2020, "A Formulation of PANS Capable of Mimicking IDDES," Int. J. Heat Fluid Flow, **86**, p. 108666.
[18] Luo, D., Yan, C., Liu, H., and Zhao, R., 2014, "Comparative Assessment of PANS and DES for Simulation of Flow Past a Circular Cylinder," J. Wind Eng. Ind. Aerodyn., **134**, pp. 65–77.
[19] Bensow, R., and van den Boogaard, M., 2019, "Using a PANS Simulation Approach for the Transient Flow Around the Japan Bulk Carrier," J. Ship Res., **63**(2), pp. 123–129.
[20] Kamble, C., and Girimaji, S., 2020, "Characterization of Coherent Structures in Turbulent Wake of a Sphere Using Partially Averaged Navier-Stokes (PANS) Simulations," Phys. Fluids, **32**(10), p. 105110.
[21] Saroha, S., Sinha, S., and Lakshmipathy, S., 2019, "Evaluation of PANS Method in Conjunction With Non-Linear Eddy Viscosity Closure Using OpenFOAM," Int. J. Numer. Methods Heat Fluid Flow, **29**(3), pp. 949–980.
[22] Saroha, S., Sinha, S., Chakraborty, K., Sinha, S., and Lakshmipathy, S., 2020, "An OpenFOAM-Based Evaluation of PANS Methodology in Conjunction With Non-Linear Eddy Viscosity: Flow Past a Heated Cylinder," J. Appl. Fluid Mech., **13**(5), pp. 1453–1469.
[23] Basara, B., Pavlovic, Z., and Girimaji, S., 2018, "A New Approach for the Calculation of the Cut-Off Resolution Parameter in Bridging Methods for Turbulent Flow Simulation," Int. J. Heat Fluid Flow, **74**, pp. 76–88.
[24] Zhang, J., Minelli, G., Rao, A., Basara, B., Bensow, R., and Krajnović, S., 2018, "Comparison of PANS and LES of the Flow Past a Generic Ship," Ocean Eng., **165**, pp. 221–236.
[25] Pereira, F., Grinstein, F., Israel, D., Rauenzahn, R., and Girimaji, S., 2021, "Modeling and Simulation of Transitional Taylor-Green Vortex Flow With Partially Averaged Navier-Stokes Equations," Phys. Rev. Fluids, **6**(5), p. 054611.
[26] Menter, F., Egorov, Y., and Rusch, D., 2006, "Steady and Unsteady Flow Modelling Using the $k-\sqrt{k}L$ Model," *ICHMT Digital Library Online*, Begell House Inc., Danbury, CT, pp. 1–20.
[27] Larsson, L., Raven, H., and Paulling, J., 2010, *Ship Resistance and Flow. Principles of Naval Architecture*, Society of Naval Architects and Marine Engineers, Jersey City, NJ.
[28] Menter, F., and Egorov, Y., 2004, "Revisiting the Turbulent Scale Equation," IUTAM Symposium on One Hundred Years of Boundary Layer Research, Göttingen, Germany, Aug. 12–14, Springer, pp. 279–290.
[29] Liebrand, R., Klapwijk, M., Lloyd, T., and Vaz, G., 2021, "Transition and Turbulence Modeling for the Prediction of Cavitating Tip Vortices," ASME J. Fluids Eng., **143**(1), p. 011202.
[30] Eça, L., Pereira, F., and Vaz, G., 2018, "Viscous Flow Simulations at High Reynolds Numbers Without Wall Functions: Is $y^+\approx 1$ Enough for the Near-Wall Cells?," Comput. Fluids, **170**, pp. 157–175.
[31] Menter, F. R., 1994, "Two-Equation Eddy-Viscosity Turbulence Models for Engineering Applications," AIAA J., **32**(8), pp. 1598–1605.
[32] Hoekstra, M., and Vaz, G., 2009, "The Partial Cavity on a 2D Foil Revisited," Proceedings of 7th International Symposium on Cavitation, MI, Aug. 16–20, pp. 1–12.
[33] Rijpkema, D., Baltazar, J., and de Campos, J., 2015, "Viscous Flow Simulations of Propellers in Different Reynolds Number Regimes," Proceedings of 4th

International Symposium on Marine Propulsors, Austin, TX, May 31-June 4, pp. 1–12.
[34] Vaz, G., Hally, D., Huuva, T., Bulten, N., Muller, P., Becchi, P., Herrer, J., Whitworth, S., Macé, R., and Korsström, A., 2015, "Cavitating Flow Calculations for the E779A Propeller in Open Water and Behind Conditions: Code Comparison and Solution Validation," Proceedings of 4th International Symposium on Marine Propulsors, Austin, TX, May 31–June 4, pp. 1–16.
[35] Vaz, G., Lloyd, T., and Gnanasundaram, A., 2017, "Improved Modelling of Sheet Cavitation Dynamics on Delft Twist 11 Hydrofoil," Proceedings of VII International Conference on Computational Methods in Marine Engineering, Nantes, Frances, June 15–17, pp. 1–14.
[36] Klaij, C., Hoekstra, M., and Vaz, G., 2018, "Design, Analysis and Verification of a Volume-of-Fluid Model With Interface-Capturing Scheme," Comput. Fluids, **170**, pp. 324–340.
[37] Eça, L., and Hoekstra, M., 2014, "A Procedure for the Estimation of the Numerical Uncertainty of CFD Calculations Based on Grid Refinement Studies," J. Comput. Phys., **262**, pp. 104–130.
[38] Lopes, R., Fernandes, E., Eça, L., Vaz, G., and Kerkvliet, M., 2020, "Coupling Two Correlation-Based Transition Models to the $k - \sqrt{k}L$ Eddy Viscosity Turbulence Model," AIAA J., **59**(5), pp. 1735–1748.
[39] Pereira, F., Eça, L., and Vaz, G., 2017, "Verification and Validation Exercises for the Flow Around the KVLCC2 Tanker at Model and Full-Scale Reynolds Numbers," Ocean Eng., **129**, pp. 133–148.
[40] Vaz, G., Jaouen, F., and Hoekstra, M., 2009, "Free-Surface Viscous Flow Computations: Validation of URANS Code FRESCO," ASME Paper No. OMAE2009-79398.
[41] Germano, M., 1992, "Turbulence: The Filtering Approach," J. Fluid Mech., **238**, pp. 325–336.
[42] Hirt, C., and Nichols, B., 1981, "Volume of Fluid (VoF) Method for the Dynamics of Free Boundaries," J. Comput. Phys., **39**(1), pp. 201–225.
[43] Schnerr, G., and Sauer, J., 2001, "Physical and Numerical Modeling of Unsteady Cavitation Dynamics," Proceedings of ICMF, 4th International Conference on Multiphase Flow, New Orleans, May 27–June 1, pp. 10–12.
[44] Reyes, D., Cooper, J., and Girimaji, S., 2014, "Characterizing Velocity Fluctuations in Partially Resolved Turbulence Simulations," Phys. Fluids, **26**(8), p. 085106.
[45] Spalart, P., and Rumsey, C., 2007, "Effective Inflow Conditions for Turbulence Models in Aerodynamic Calculations," AIAA J., **45**(10), pp. 2544–2553.
[46] Lopes, R., Eça, L., Vaz, G., and Kerkvliet, M., 2021, "Assessing Numerical Aspects of Transitional Flow Simulations Using the RANS Equations," Int. J. Comput. Fluid Dyn., **35**(3), pp. 1–22.
[47] Klapwijk, M., Lloyd, T., Vaz, G., and Van Terwisga, T., 2021, "On the Use of Synthetic Inflow Turbulence for Scale-Resolving Simulations of Wetted and Cavitating Flows," Ocean Eng., **228**, p. 108860.
[48] Lopes, R., 2021, "Simulation of Transition From Laminar to Turbulent Regime in Practical Applications of Incompressible Flow," Ph.D. thesis, Universidade de Lisboa, Instituto Superior Técnico, Portugal.
[49] Xu, C.-Y., Zhang, T., Yu, Y.-Y., and Sun, J.-H., 2019, "Effect of Von Karman Length Scale in Scale Adaptive Simulation Approach on the Prediction of Supersonic Turbulent Flow," Aerosp. Sci. Technol., **86**, pp. 630–639.
[50] Klapwijk, M., Lloyd, T., Vaz, G., and Van Terwisga, T., 2019, "PANS Simulations: Low Versus High Reynolds Number Approach," Proceedings of VIII International Conference on Computational Methods in Marine Engineering, Göthenburg, Sweden, May 13–15, pp. 48–59.
[51] Moser, R., Kim, J., and Mansour, N., 1999, "Direct Numerical Simulation of Turbulent Channel Flow Up to $Re_\tau = 590$," Phys. Fluids, **11**(4), pp. 943–945.
[52] Pereira, F., Eça, L., Vaz, G., and Girimaji, S., 2018, "Challenges in Scale-Resolving Simulations of Turbulent Wake Flows With Coherent Structures," J. Comput. Phys., **363**, pp. 98–115.
[53] Zhang, Y., 2017, "Critical Transition Reynolds Number for Plane Channel Flow," Appl. Math. Mech., **38**(10), pp. 1415–1424.
[54] Pennings, P., Westerweel, J., and Van Terwisga, T., 2015, "Flow Field Measurement Around Vortex Cavitation," Exp. Fluids, **56**(11), p. 206.
[55] Xie, Z.-T., and Castro, I., 2008, "Efficient Generation of Inflow Conditions for Large Eddy Simulation of Street-Scale Flows," Flow Turbul. Combust., **81**(3), pp. 449–470.
[56] Lloyd, T., Vaz, G., Rijpkema, D., and Reverberi, A., 2017, "Computational Fluid Dynamics Prediction of Marine Propeller Cavitation Including Solution Verification," Proceedings of 5th Symposium on Marine Propulsion, Espoo, Finland, June 12–15, pp. 58–70.
[57] Asnaghi, A., Svennberg, U., and Bensow, R., 2020, "Large Eddy Simulations of Cavitating Tip Vortex Flows," Ocean Eng., **195**, p. 106703.
[58] Reverberi, A., 2016, "Cavitation Modelling of E779A Propeller Accounting for Transition Effects," MARIN, Wageningen, the Netherlands, Technical Report.
[59] Bosschers, J., 2018, "Propeller tip-vortex cavitation and its broadband noise," Ph.D. thesis, University of Twente, the Netherlands.